Distinct learning-induced changes in stimulus selectivity and interactions of GABAergic interneuron classes in visual cortex

Adil G. Khan[1, 4]*†, Jasper Poort[2]*†, Angus Chadwick[3]*, Antonin Blot[1]*, Maneesh Sahani[3], Thomas D. Mrsic-Flogel[1, 2]†, Sonja B. Hofer[1, 2]†

1. Biozentrum, University of Basel, Basel, Switzerland
2. Sainsbury Wellcome Centre for Neural Circuits and Behaviour, University College London, London, UK
3. Gatsby Computational Neuroscience Unit, University College London, London, UK
4. Present address: Centre for Developmental Neurobiology, Institute of Psychiatry, Psychology and Neuroscience, King's College London, London, UK

* Authors contributed equally

† Corresponding authors

Correspondence to: S.B.H. s.hofer@ucl.ac.uk, T.D.M-F. t.mrsic-flogel@ucl.ac.uk, A.G.K. khan.adil@kcl.ac.uk or J.P. j.poort@ucl.ac.uk

Summary

How learning enhances neural representations for behaviorally relevant stimuli via activity changes of cortical cell types remains unclear. We simultaneously imaged responses of pyramidal cells (PYR), and parvalbumin (PV), somatostatin (SOM), and vasoactive intestinal peptide (VIP) inhibitory interneurons in primary visual cortex while mice learned to discriminate visual patterns. Learning increased selectivity for task-relevant stimuli of PYR, PV and SOM subsets but not VIP cells. Strikingly, PV neurons became as selective as PYR cells, and their functional interactions reorganized leading to the emergence of stimulus-selective PYR-PV ensembles. Conversely, SOM activity became strongly decorrelated from the network, and PYR-SOM coupling before learning predicted selectivity increases in individual PYR cells. Thus, learning differentially shapes the activity and interactions of multiple cell classes; while SOM inhibition may gate selectivity changes, PV interneurons become recruited into stimulus-specific ensembles and provide more selective inhibition as the network becomes better at discriminating behaviorally relevant stimuli.

Introduction

Learning exerts a powerful influence on how cortical circuits process sensory information. Cortical representations become more selective and better at discriminating sensory stimuli as they acquire behavioral relevance during learning[1–5]. These improvements in sensory coding take place in richly interconnected networks containing principal excitatory neurons as well as multiple classes of GABAergic interneurons, each with distinct molecular, cellular and connectional properties[6,7]. Yet how learning changes the responses and interactions of excitatory and inhibitory cell classes, and how these changes might relate to improvements in sensory coding, remains poorly understood.

Specific classes of inhibitory interneurons have been implicated in plasticity of cortical circuits during learning[8–13]. In principle, inhibitory neurons could gate the plasticity of inputs onto pyramidal cells[14–18,11] as well as inhibit or disinhibit their responses to specific sensory stimuli[10–13,19]. However, it is not known whether learning can enhance the response selectivity for behaviorally relevant stimuli in specific classes of interneurons and thus provide more stimulus-specific inhibition to the network. Moreover, each interneuron class has been suggested to act as a functionally (and thus computationally) homogeneous unit during sensory or behavioral events[20–23,12,24], but it is not clear whether learning leads to homogeneous response changes within each interneuron class. Finally, due to the dense connectivity of cortical networks, any change in responses in one group of interneurons could lead to complex changes in responses of neurons belonging to other classes. However, only a few studies have measured or modeled activity of multiple cell classes concurrently[25,24,19]. As a result, the nature of interactions between different cell classes, and how they change with learning, remains poorly understood.

To address these questions, we imaged simultaneously the responses of four classes of cortical neurons: putative pyramidal cells (PYR), and parvalbumin (PV), somatostatin (SOM), and vasoactive intestinal peptide (VIP) expressing interneurons in layer 2/3 (L2/3) of the primary visual cortex (V1) before and after mice learned a visual discrimination task. In each cell class we observed heterogeneous responses to behaviorally relevant visual stimuli as well as diverse response changes with learning. Most strikingly, learning led to a pronounced increase in the stimulus selectivity of PV cells. A linear autoregressive system model revealed a reorganization of interactions between PYR and PV cells consistent with the emergence of stimulus specific PYR-PV subnetworks. In contrast, SOM cells became decorrelated from the local network during learning, and the degree of correlation with the SOM population before

learning predicted the extent of selectivity increase in PYR cells, suggesting that SOM cells gate response plasticity. These results reveal concerted changes in interactions between cortical cell classes during learning, and suggest differential roles of SOM and PV cells in induction and expression of response changes that lead to more selective processing of relevant stimuli.

Results

To understand how learning changes the responses of different cell types in V1, we trained mice to perform a visual discrimination task in a virtual reality environment[5] (**Fig. 1a**). Head-fixed mice learnt a go-no go discrimination task (**Fig. 1b**) in which they ran through a virtual approach corridor where the walls displayed a short stretch of circle patterns followed by gray for a random distance, before they were abruptly presented with one of two grating patterns. Mice were rewarded for licking a reward spout only in response to vertical gratings. No punishment was given for licking in response to angled gratings (40° relative to vertical). All mice learnt to discriminate the two stimuli, starting at chance performance (behavioral d' close to zero) and reaching a threshold criterion of d' > 2.0 within 9 days (~85% accuracy, **Fig. 1c**, sign test, P = 0.008, N = 8 mice).

We used viral vectors to express the calcium indicator GCaMP6f[26] in V1 and recorded responses of populations of L2/3 cells during the task before and after learning using two-photon calcium imaging. We then re-identified the same neurons in co-registered, immunohistochemically stained brain sections of the same animals and detected simultaneously imaged PV-positive, SOM-positive and VIP-positive interneurons[27–29] (**Fig. 1d, Supplementary Fig. 1**). Immuno-unlabeled cells were classified as putative PYR cells[30].

Response heterogeneity within and across interneuron classes

We first characterized the responses of the PYR, PV, SOM and VIP neurons while mice engaged in visual discrimination. The activity of many cells in each class was modulated by the onset of the task-relevant grating stimuli (**Fig. 1e, Supplementary Fig. 2a, b**). While on average VIP calcium signals peaked close to stimulus onset and decreased abruptly thereafter, the responses of PYR, PV and SOM cells typically increased after stimulus onset (**Fig. 1f, Supplementary Fig. 2c**). The average stimulus-triggered response profiles of PYR and PV cells were most similar to each other, while SOM and VIP cells exhibited opposing response profiles (**Fig. 1f, g, Supplementary Fig. 2c, d**).

Notably, responses of individual neurons within each cell class were highly heterogeneous, including stimulus-evoked increases and decreases in activity with diverse time-courses (**Fig. 1e, Supplementary Fig. 2a, b**). Within-class diversity was also apparent in responses triggered by the onset of running, and the delivery of reward or an odor (**Supplementary Fig. 3**). Thus, response profiles are broadly different between cell classes, but also heterogeneous within each cell class.

Learning increases stimulus selectivity of specific cell classes

During learning, the responses to task-relevant grating stimuli changed in subsets of neurons from all cell classes, including both increases and decreases in response amplitude (**Supplementary Fig. 4)**, as well as changes in the average population response of each class (**Supplementary Fig. 4a, d**). These response changes modified stimulus selectivity in individual cells to varying degrees (difference in the responses to the vertical and angled grating stimuli normalized by response variability, see Online Methods, **Fig. 2a, b**). On average, PYR cells significantly increased their stimulus selectivity, as reported previously (average absolute selectivity pre-learning, 0.31 ± 0.32 (mean ± std), post-learning 0.41 ± 0.45, sign test, $P < 10^{-7}$, N = 1249)[5]. Notably, selectivity also increased strongly in PV cells, in which calcium responses to the task-relevant stimuli became as selective as in PYR cells (**Fig. 2b-d**, **Supplementary Fig. 5a**; pre-learning 0.25 ± 0.20, post-learning 0.43 ± 0.38, sign test, P = 0.002, N = 132). Although on average the selectivity of SOM interneurons did not change significantly (pre-learning 0.27 ± 0.18, post-learning 0.40 ± 0.46, P = 0.51, N = 58; **Fig. 2d**), 21% of SOM cells became significantly more selective during learning (**Fig. 2b, c**). In contrast, VIP cells were poorly responsive to and selective for the grating stimuli, and remained so after learning (pre-learning 0.19 ± 0.17, post-learning 0.19 ± 0.16, P = 1.00, N = 175; **Fig. 2b-d**). Changes in eye position, pupil size, eye movements, running and licking could not account for the increased selectivity of responses after learning (**Supplementary Fig. 5b-i**). Furthermore, the increased response selectivity was specific to the task-relevant grating stimuli and was not observed in the approach corridor (**Supplementary Fig. 5j**).

To test whether differences across cell types in selectivity for task-relevant stimuli might have resulted from different nonlinearities in the relationship between a neuron's firing rate and calcium concentration, we performed loose-patch recordings of spiking activity while simultaneously imaging GCaMP6 calcium fluorescence in the three interneuron classes in visual cortex slices. We found a near-linear relationship between firing rate and the associated average calcium fluorescence changes in all interneuron classes (**Fig. 2e, Supplementary**

Fig. 6, PV = 13, SOM = 17 and VIP = 11 cells). The slope of this relationship was lower for PV cells than for SOM and VIP cells, possibly reflecting different calcium buffering capacities of these GABAergic populations[31]. The relationship between firing rate and fluorescence changes allowed us to infer the firing rates of imaged cells based on measured calcium transients on each trial. The selectivity values obtained from the inferred firing rate closely matched those obtained from calcium signals in each interneuron class (**Fig. 2f**). Thus, the observed changes in selectivity during learning were unlikely to arise from differences in calcium signal nonlinearities of the three interneuron classes.

The increased selectivity of PV cells for the grating stimuli was unexpected given that these interneurons are thought to broadly integrate the activity of surrounding PYR cells[27,32–34] (but see Wilson et. al.[29]), thus providing local inhibition proportional to the average local activity. Indeed, we observed a positive correlation between PV cell selectivity and the selectivity of average PYR cell activity (within 100 μm from each PV cell) before learning (**Fig. 2g** top, slope = 0.2, confidence intervals (CI) 0.14 to 0.26, R = 0.49). However, the slope and correlation coefficient of this relationship decreased with learning (**Fig. 2g** bottom, slope = 0.05, CI 0.02 to 0.10, reduction in slope bootstrap test $P < 10^{-4}$, R = 0.26). Thus, the emergence of selective responses for behaviorally relevant stimuli in PV cells was associated with their activity becoming more independent from the average stimulus preference of the surrounding PYR cells. In contrast, the relationship between the selectivity of SOM cells and surrounding PYR cells remained constant with learning (**Fig. 2h,** slope before learning = 0.14, CI 0.04 to 0.24, R = 0.38, and after learning slope = 0.15, CI 0.05 to 0.25, R = 0.51, P > 0.05).

Learning reorganizes cell type-specific interactions

These results suggest that improvements in response selectivity during learning are associated with a restructuring of firing interdependencies between different cell types in visual cortex. Specifically, PV cells might become more strongly influenced by external (top down or bottom up) inputs and driven less by surrounding PYR cells after learning. Alternatively, individual PV cells might acquire more selective input from subsets of PYR cells with specific stimulus-preferences during learning, leading them to respond more selectively. Both hypotheses predict a decreased dependence of PV firing on the average local network selectivity but with distinct changes in firing interdependencies between different cell types over learning. If a cell type were to decouple from the surrounding network and become more strongly influenced by non-local inputs, its co-fluctuations with neighboring cells would

decrease substantially. This would not be the case if a cell developed selective associations with neighboring cells of a given stimulus preference.

To distinguish between these hypotheses, we computed noise correlations during the grating stimulus period between pairs of neurons within and across cell classes, before and after learning (**Fig. 3, Supplementary Fig. 7**). Noise correlations reflect the stimulus-independent trial-to-trial covariability of responses (**Fig. 3a, b**), and thus provide an estimate of mutual connectivity and shared inputs[35–37]. We found that learning decreased noise correlations both within and between cell classes (sign test, all Ps < 10^{-4}, with the exception of SOM-SOM cell pairs, P = 0.35), indicating that firing in the network became more independent (**Fig. 3c**). Notably, the activity of SOM cells became strongly decorrelated from that of PYR, PV and VIP cells, while, in contrast, the firing of PV and VIP cells exhibited less decorrelation (**Fig. 3d**). Thus, the responses of SOM cells in particular became uncoupled from the local network during learning. Changes in eye position, pupil size, eye movements, running, licking, or reductions in response strength could not account for the observed changes in noise correlations (**Supplementary Fig. 8**). We further verified that our estimate of noise correlation was not strongly influenced by trial-to-trial variability in running speed, visual stimulus and eye position (**Supplementary Fig. 9**).

To what extent do modifications in functional interactions across cell types underlie changes in stimulus selectivity of individual neurons during learning? We fit a multivariate autoregressive (MVAR) linear dynamical system model (**Fig. 4a**) to the data, which predicted the activity of each cell based on two main components: (1) a contribution from the weighted activity of the simultaneously recorded population in the preceding time bin (the recurrent input), and (2) a contribution from a trial-invariant stimulus-locked input (the stimulus input)**.** When the MVAR model is fit to the data, the interaction weights organize to best capture the covariance of the responses across the population, whereas the stimulus-related inputs adjust, given these interaction weights, to exactly replicate the average response profile of each cell (see Online Methods, **Fig. 4b**). The interaction weights should not be interpreted directly in terms of synaptic efficacies, but rather as effective influences over timescales of ~100 ms, as determined by the imaging rate of 8 Hz.

We also included an input proportional to running speed in the model, but this had a negligible contribution to the responses (**Supplementary Fig. 10a**). Any remaining unexplained response variability was assigned to a residual term.

To test how accurately the data were captured by the MVAR model, we compared it to models with different forms of dynamics using cross validation. When tested on held-out data, the MVAR model outperformed both simpler models without interactions, as well as more complex models with time-varying interaction weights (**Supplementary Fig. 10b, c**, Online Methods). The interaction terms in the MVAR model were essential to capture the coherent trial-to-trial response fluctuations of neural activity in the data. Simulated network responses with all interaction weights deleted (set to zero, see Online Methods), led to average noise correlations that were substantially smaller than those in the experimental data (**Fig. 4c,** mean over all cells 0.013 ± 0.043 from 0.077 ± 0.09, also **Supplementary Fig. 10d** for fit to pre-learning data) and the structure of pairwise noise correlations was re-organized entirely (**Fig. 4d** top, observed versus weights deleted: R^2 = -0.18). By contrast, simulating responses with the residuals shuffled, thus eliminating residual coherent fluctuations *not* captured by the interaction weights (see Online Methods), had a negligible effect (**Fig. 4c,** mean over all cells 0.058 ± 0.07 from 0.077 ± 0.09; **Fig. 4d** bottom, observed versus residuals shuffled: R^2 = 0.59).

Although the model was blind to cell type, we observed cell-class-specific differences in the interaction weights and their changes over learning (**Supplementary Fig. 10e**). Manipulating the interaction weights, which are determined only by the trial-to-trial fluctuations and independent of the mean response profiles (see Online Methods), allowed us to determine the extent to which the stimulus selectivity of different interneuron classes can be explained by functional interactions within the local network. We simulated the responses of the population with all interaction weights intact or deleted (**Fig. 4e, f**, see Online Methods). Before learning, deleting interaction weights led to a small but significant reduction in the absolute selectivity of PV and SOM cells (**Fig. 4e**; pre-learning P-values < 10^{-2}, sign test, see **Supplementary Fig. 11a** for effects of weight deletions on PYR and VIP cell selectivity). After learning, deleting interaction weights resulted in a larger reduction in selectivity of PV cells (**Fig. 4f**; post-learning P < 10^{-8}, sign test; change in slope between values with intact vs deleted weights after learning, P < 10^{-4}, bootstrap test). In contrast, SOM cell selectivity was not affected by weight deletion after learning (**Fig. 4f**, post-learning P = 0.51, sign test; slope comparison, P = 0.11, bootstrap test). Together, these results indicate that while PV selectivity becomes more dependent on local network interactions, the stimulus selectivity of SOM neurons becomes less dependent on the local network, consistent with the decorrelation of SOM responses during learning (**Fig. 3c**).

When manipulating inputs from different cell classes onto PV or SOM neurons, we found that specifically deleting PYR to PV interaction weights exerted a particularly strong effect on PV selectivity after learning (**Fig. 4g, Supplementary Fig. 11b**, pre- to post-learning change P = 0.02, sign test) while the effect of other cell-type specific weight deletions on selectivity did not change with learning for PV or SOM cells (**Fig. 4g, h**, all P-values pre- vs post-learning > 0.05, sign test). These results predict a reorganization of local PYR interaction weights onto PV cells in visual cortex during learning. Indeed, we found that after learning, PYR to PV interaction weights were significantly higher between cells that preferred the same grating stimulus compared to pairs of cells with disparate preferences for the task-relevant grating stimuli (**Fig. 4j**, P-values < 10^{-3}, Wilcoxon rank-sum test). In keeping with previous results[35,37], PYR to PYR interaction weights already showed this functional specificity before learning, while no such differences were observed either pre- or post-learning for PYR to SOM weights (**Supplementary Fig. 11c**). However, similar to the weights from PYR to PV cells, PV to PYR and PV to PV interaction weights also diverged after learning between cell pairs with the same versus different visual stimulus preference (**Supplementary Fig. 11c**, P-values < 10^{-3}, Wilcoxon rank-sum test). Positive weights of inhibitory connections are expected at the sampling rate of our recordings (8Hz), as excitation and inhibition in cortical networks fluctuate coherently over longer timescales, with negative correlations emerging only at very short timescales of several milliseconds[38,39]. Thus, selective interactions between subsets of PV and PYR cells with similar stimulus preference developed during learning, consistent with the emergence of stimulus-selective PYR-PV subnetwork activity (**Fig. 4k**). Moreover, the model further revealed that stimulus-related inputs onto PV cells were not required to change during learning in order to account for their increased selectivity during learning (**Supplementary Fig. 11e**, Online Methods), indicating that the emergent preference of PV cells for task-relevant stimuli may be fully accounted for by changes in inputs from the local network.

Notably, the increased selectivity of PV cells may further contribute to PYR cell selectivity changes. Specifically, deletion of PV to PYR weights significantly reduced PYR selectivity, and this effect was greater after learning (**Fig. 4i,** P < 10^{-3}, sign test). In contrast, the effects of deleting SOM and PYR cell weights onto PYR cells did not change with learning (P-values > 0.05). Taken together, these results indicate a key functional difference between PV and SOM interneurons. Post-learning, PV cells may integrate activity more selectively from local PYR cells and in turn provide more selective inhibition to the network after learning. In contrast, SOM cells appear to become uncoupled from the local network and might be influenced more

by external signals after learning.

Correlation with SOM cells predicts selectivity changes

Pairing of top-down and bottom-up inputs arriving in apical and basal dendrites respectively is believed to be important for forming new associations[40], and may contribute to increased stimulus selectivity of PYR cells during learning. As SOM cells preferentially target the dendrites of PYR cells they could gate the influence of top-down, task-related signals arriving in layer 1[41,40,11,42]. Those PYR cells that experience SOM mediated dendritic inhibition synchronous with bottom up stimulus-related drive may be prevented from pairing top down and bottom up inputs, and thus may not exhibit learning-related selectivity changes. We selected PYR cells that were highly correlated with the average SOM population activity before learning (top 20th percentile), and found that this subset of PYR cells showed very low selectivity increases during learning (**Fig. 5a**, right, **Fig. 5b**). Conversely, PYR cells that exhibited the lowest noise correlations with the SOM population (bottom 20th percentile) showed a significantly larger learning-induced increase in selectivity (**Fig. 5a**, left, **Fig. 5b,** P=0.001 Wilcoxon rank-sum test. The result was similar when only including cells that were non-selective before learning, P = 0.039, see Online Methods). This dependence of changes in PYR cell selectivity on the extent of coupling with the SOM population was not apparent after learning (P = 0.4), and neither could PYR, PV or VIP population coupling predict selectivity changes in PYR cells (**Fig. 5b**, all P-values pre- and post-learning > 0.2). PV cells, which also significantly increased selectivity with learning, displayed no such relationship with SOM cell population activity (**Fig. 5c**, all P-values > 0.4). Thus, the degree to which PYR neurons increase their selectivity during learning can be predicted from their correlation with the SOM cell population before learning.

Discussion

Previous studies in various cortical areas have suggested that interneurons of a given molecularly defined class can act as a relatively homogenous functional unit during specific sensory or behavioral events, including high activity correlations between cells of the same class[20–23,12,24,13]. We found that activity correlations across cell classes (e.g. PV-VIP cell pairs) can be as high as those within a class (e.g. PV-PV, VIP-VIP pairs[24]). This implies that functional cell ensembles or subnetworks can span multiple cell types. Importantly, however, we observed a substantial within cell-class heterogeneity in responses aligned to onsets of

behaviorally relevant grating stimuli, running, reward and odor delivery, including response increases and decreases, as well as in learning-related response changes of PV, SOM and VIP interneurons in visual cortex. The fact that neurons within each cell class can be functionally diverse may not be surprising given that each molecularly defined class comprises cells with various morphologies, network connectivity and intrinsic properties[6,43,7,44]. The challenge for future studies is to establish the extent to which the heterogeneous behavior of single cells is captured by the diversity of cell types within an interneuron class and to determine any brain-state and region-specific differences in their activity.

We demonstrate that learning changes the selectivity and functional interactions of multiple classes of inhibitory interneurons in V1. Hence the relationship between neurons within and across cell classes and their contribution to network function is not static, but it can change with experience. We found that PV cells were poorly selective for task-relevant grating stimuli before learning. This is consistent with observations that PV cells, on average, broadly integrate inputs from their neighbors and therefore display broad visual stimulus tuning in mouse V1[27,32–34]. After learning, however, PV cells became selective and their tuning was less related to the preference of the average surrounding network of PYR cells. This result implies a rearrangement of interactions between PYR and PV cells, which were captured quantitatively by a linear dynamical system model. The model provided two significant insights. First, the origins of noise correlations in a neural network have been debated. Here we show that noise correlations can to a large extent be accounted for by the local functional interactions in a model with simple linear dynamics. Second, PYR to PV interaction weights became specific for stimulus preference during learning and significantly contributed to PV selectivity changes. Together, the model and data therefore suggest that learning induces plasticity in excitatory inputs onto PV cells, with stronger weights shared by cells preferring the same stimuli (note that the model cannot exclude the possibility that feedforward or feedback inputs onto PV cells also change during learning). This implies that PV cells can adjust which local excitatory inputs they sample subject to experience, leading to the emergence of PYR-PV ensembles selective for task-relevant stimuli. These effects were cell-class specific and not observed in interactions between PYR and SOM cells. Rather, SOM cells became decorrelated from other cell classes in the local network over the course of learning, and their response selectivity became less dependent on local interactions. Their activity during the task might therefore increasingly reflect signals from long-range inputs[45,10]. In the future, these insights could be tested directly by assessing the local and

long-range connectivity of PYR, PV and SOM neurons with specific response properties[33,46] in naive and expert mice.

Irrespective of its origin, the increased selectivity of PV cells implies an increase in the amount of selective inhibition in the local network, which may further sharpen cortical representations of task-relevant sensory stimuli[47]. In contrast, VIP cells remained unselective throughout learning, suggesting they do not play a direct role in shaping selective PYR cell responses after learning. This indicates that specific cell classes can be insulated from otherwise widespread network changes. VIP neurons may instead contribute to the decorrelation of SOM cell activity from the local network[48,49,24,21]

Dendrite-targeting SOM interneurons have been shown to be important for learning, and exhibit changes in their activity and bouton density in concert with learning-related changes in PYR cells[50,11,10,12]. We find that in naïve animals the degree of correlated activity with the SOM cell population predicts how strongly PYR neurons increase their selectivity during learning. Our results are consistent with the notion that SOM cells gate learning-related plasticity during the visual discrimination task by preventing the pairing of top-down and bottom-up inputs arriving in apical and basal dendrites respectively. Those PYR cells that receive highly correlated SOM inhibition are thus unable to increase their stimulus selectivity[40,11,10]. Conversely, low correlations with SOM cells were permissive of plasticity in PYR cells (**Fig. 5**). Indeed, the strong decorrelation of SOM cells from the rest of the network during learning may serve as a mechanism to increase plasticity of V1 circuits as visual stimuli become behaviorally relevant. Thus sensory cortical circuits may become primed to more readily undergo additional learning-related changes, for instance to facilitate further associations between visual stimuli and task-related signals.

Taken together, our results highlight the existence of functional diversity across and within three molecularly defined cell classes of interneurons. We find that learning-induced changes in cortical circuits are highly interdependent, involving interactions across multiple cell classes to enable more selective processing and increased discriminability of behaviorally relevant sensory stimuli.

Author contributions

AGK, JP, TDMF and SBH designed the experiments. AGK and JP built the setup for imaging experiments in behaving mice, performed the experiments, and analyzed the data. AC

developed the MVAR model, performed the model-based data analysis and wrote the modeling results with supervision from MS and help from JP. AB performed the immunostaining and did the simultaneous calcium imaging and loose patch recordings. AB, AGK and JP established and performed the post-hoc cell matching procedure. AGK, JP, TDMF and SBH wrote the paper, with inputs from all authors.

Acknowledgments

We thank P Znamenskiy and G Keller for discussions of the results in this manuscript. We thank A Keller for advice on the immunostaining protocol, and M Li for technical assistance. We thank the GENIE Program and Janelia Research Campus of the Howard Hughes Medical Institute for making GCaMP6 material available. This work was supported by the European Research Council (SBH, HigherVision 337797, TDM-F, NeuroV1sion 616509), the Swiss National Science Foundation (SBH, 31003A_169525), the Marie Curie Actions of the European Union's FP7 program (JP, 332141 and AGK, 301742), an Ambizione grant from the SNSF (AGK), the UCL Excellence fellowship (JP), the EMBO long-term postdoc fellowship (AB), the Gatsby Charitable Foundation (MS), the Simons Foundation (MS, SCGB 323228, 543039) and Biozentrum core funds (University of Basel).

Competing interests

The authors declare no competing financial or non-financial interests

References

1. Recanzone, G. H., Schreiner, C. E. & Merzenich, M. M. Plasticity in the frequency representation of primary auditory cortex following discrimination training in adult owl monkeys. *J. Neurosci.* **13,** 87–103 (1993).
2. Schoups, A., Vogels, R., Qian, N. & Orban, G. Practising orientation identification improves orientation coding in V1 neurons. *Nature* **412,** 549–553 (2001).
3. Yang, T. & Maunsell, J. H. The effect of perceptual learning on neuronal responses in monkey visual area V4. *J. Neurosci.* **24,** 1617–1626 (2004).
4. Yan, Y. *et al.* Perceptual training continuously refines neuronal population codes in primary visual cortex. *Nat. Neurosci.* **17,** 1380–1387 (2014).
5. Poort, J. *et al.* Learning Enhances Sensory and Multiple Non-sensory Representations in Primary Visual Cortex. *Neuron* **86,** 1478–1490 (2015).
6. Markram, H. *et al.* Interneurons of the neocortical inhibitory system. *Nat.Rev.Neurosci.* **5,** 793–807 (2004).
7. Kepecs, A. & Fishell, G. Interneuron cell types are fit to function. *Nature* **505,** 318–326 (2014).
8. Letzkus, J. J. *et al.* A disinhibitory microcircuit for associative fear learning in the auditory cortex. *Nature* **480,** 331–335 (2011).
9. Donato, F., Rompani, S. B. & Caroni, P. Parvalbumin-expressing basket-cell network plasticity induced by experience regulates adult learning. *Nature* **504,** 272–276 (2013).
10. Makino, H. & Komiyama, T. Learning enhances the relative impact of top-down processing in the visual cortex. *Nat. Neurosci.* **18,** 1116–1122 (2015).
11. Chen, S. X., Kim, A. N., Peters, A. J. & Komiyama, T. Subtype-specific plasticity of inhibitory circuits in motor cortex during motor learning. *Nat. Neurosci.* **18,** 1109–1115 (2015).
12. Kato, H. K., Gillet, S. N. & Isaacson, J. S. Flexible Sensory Representations in Auditory Cortex Driven by Behavioral Relevance. *Neuron* **88,** 1027–1039 (2015).

13. Sachidhanandam, S., Sermet, B. S. & Petersen, C. C. H. Parvalbumin-Expressing GABAergic Neurons in Mouse Barrel Cortex Contribute to Gating a Goal-Directed Sensorimotor Transformation. *Cell Rep.* (2016). doi:10.1016/j.celrep.2016.03.063
14. Fagiolini, M. & Hensch, T. K. Inhibitory threshold for critical-period activation in primary visual cortex. *Nature* **404,** 183–186 (2000).
15. Froemke, R. C., Merzenich, M. M. & Schreiner, C. E. A synaptic memory trace for cortical receptive field plasticity. *Nature* **450,** 425–429 (2007).
16. Chen, J. L. *et al.* Structural basis for the role of inhibition in facilitating adult brain plasticity. *Nat. Neurosci.* **14,** 587–594 (2011).
17. van Versendaal, D. *et al.* Elimination of Inhibitory Synapses Is a Major Component of Adult Ocular Dominance Plasticity. *Neuron* **74,** 374–383 (2012).
18. Kuhlman, S. J. *et al.* A disinhibitory microcircuit initiates critical-period plasticity in the visual cortex. *Nature* **501,** 543–546 (2013).
19. Kuchibhotla, K. V. *et al.* Parallel processing by cortical inhibition enables context-dependent behavior. *Nat. Neurosci.* **20,** 62–71 (2017).
20. Kvitsiani, D. *et al.* Distinct behavioural and network correlates of two interneuron types in prefrontal cortex. *Nature* **498,** 363–366 (2013).
21. Pi, H.-J. *et al.* Cortical interneurons that specialize in disinhibitory control. *Nature* **503,** 521–524 (2013).
22. Hangya, B., Pi, H.-J., Kvitsiani, D., Ranade, S. P. & Kepecs, A. From circuit motifs to computations: mapping the behavioral repertoire of cortical interneurons. *Curr. Opin. Neurobiol.* **26,** 117–124 (2014).
23. Pinto, L. & Dan, Y. Cell-Type-Specific Activity in Prefrontal Cortex during Goal-Directed Behavior. *Neuron* **87,** 437–450 (2015).
24. Karnani, M. M. *et al.* Cooperative Subnetworks of Molecularly Similar Interneurons in Mouse Neocortex. *Neuron* **90,** 86–100 (2016).

25. Litwin-Kumar, A., Rosenbaum, R. & Doiron, B. Inhibitory stabilization and visual coding in cortical circuits with multiple interneuron subtypes. *J. Neurophysiol.* jn.00732.2015 (2016). doi:10.1152/jn.00732.2015

26. Chen, T.-W. *et al.* Ultrasensitive fluorescent proteins for imaging neuronal activity. *Nature* **499,** 295–300 (2013).

27. Kerlin, A. M., Andermann, M. L., Berezovskii, V. K. & Reid, R. C. Broadly tuned response properties of diverse inhibitory neuron subtypes in mouse visual cortex. *Neuron* **67,** 858–871 (2010).

28. Keller, A. J. & Martin, K. A. C. Local Circuits for Contrast Normalization and Adaptation Investigated with Two-Photon Imaging in Cat Primary Visual Cortex. *J. Neurosci.* **35,** 10078–10087 (2015).

29. Wilson, D. E. *et al.* GABAergic Neurons in Ferret Visual Cortex Participate in Functionally Specific Networks. *Neuron* **93,** 1058–1065.e4 (2017).

30. Rudy, B., Fishell, G., Lee, S. & Hjerling-Leffler, J. Three groups of interneurons account for nearly 100% of neocortical GABAergic neurons. *Dev. Neurobiol.* **71,** 45–61 (2011).

31. Hu, H., Gan, J. & Jonas, P. Fast-spiking, parvalbumin+ GABAergic interneurons: From cellular design to microcircuit function. *Science* **345,** 1255263 (2014).

32. Bock, D. D. *et al.* Network anatomy and in vivo physiology of visual cortical neurons. *Nature* **471,** 177–182 (2011).

33. Hofer, S. B. *et al.* Differential connectivity and response dynamics of excitatory and inhibitory neurons in visual cortex. *Nat. Neurosci.* **14,** 1045–1052 (2011).

34. Scholl, B., Pattadkal, J. J., Dilly, G. A., Priebe, N. J. & Zemelman, B. V. Local Integration Accounts for Weak Selectivity of Mouse Neocortical Parvalbumin Interneurons. *Neuron* **87,** 424–436 (2015).

35. Ko, H. *et al.* Functional specificity of local synaptic connections in neocortical networks. *Nature* **473,** 87–91 (2011).

36. Cohen, M. R. & Kohn, A. Measuring and interpreting neuronal correlations. *Nat. Neurosci.* **14,** 811–819 (2011).

37. Cossell, L. *et al.* Functional organization of excitatory synaptic strength in primary visual cortex. *Nature* **518,** 399–403 (2015).

38. Tsodyks, M. V., Skaggs, W. E., Sejnowski, T. J. & McNaughton, B. L. Paradoxical Effects of External Modulation of Inhibitory Interneurons. *J. Neurosci.* **17,** 4382–4388 (1997).

39. Ozeki, H., Finn, I. M., Schaffer, E. S., Miller, K. D. & Ferster, D. Inhibitory Stabilization of the Cortical Network Underlies Visual Surround Suppression. *Neuron* **62,** 578–592 (2009).

40. Larkum, M. A cellular mechanism for cortical associations: an organizing principle for the cerebral cortex. *Trends Neurosci.* **36,** 141–151 (2013).

41. Silberberg, G. & Markram, H. Disynaptic inhibition between neocortical pyramidal cells mediated by Martinotti cells. *Neuron* **53,** 735–746 (2007).

42. Takahashi, N., Oertner, T. G., Hegemann, P. & Larkum, M. E. Active cortical dendrites modulate perception. *Science* **354,** 1587–1590 (2016).

43. Runyan, C. A. & Sur, M. Response Selectivity Is Correlated to Dendritic Structure in Parvalbumin-Expressing Inhibitory Neurons in Visual Cortex. *J. Neurosci.* **33,** 11724–11733 (2013).

44. Jiang, X. *et al.* Principles of connectivity among morphologically defined cell types in adult neocortex. *Science* **350,** aac9462 (2015).

45. Zhang, S. *et al.* Selective attention. Long-range and local circuits for top-down modulation of visual cortex processing. *Science* **345,** 660–665 (2014).

46. Wertz, A. *et al.* Single-cell–initiated monosynaptic tracing reveals layer-specific cortical network modules. *Science* **349,** 70–74 (2015).

47. Harris, K. D. & Mrsic-Flogel, T. D. Cortical connectivity and sensory coding. *Nature* **503,** 51–58 (2013).

48. Pfeffer, C. K., Xue, M., He, M., Huang, Z. J. & Scanziani, M. Inhibition of inhibition in visual cortex: the logic of connections between molecularly distinct interneurons. *Nat. Neurosci.* **16,** 1068–1076 (2013).

49. Lee, S., Kruglikov, I., Huang, Z. J., Fishell, G. & Rudy, B. A disinhibitory circuit mediates motor integration in the somatosensory cortex. *Nat. Neurosci.* **16,** 1662–1670 (2013).

50. Cichon, J. & Gan, W.-B. Branch-specific dendritic Ca2+ spikes cause persistent synaptic plasticity. *Nature* **520,** 180–185 (2015).

Online Methods

Experimental procedures for the behavioral task, surgery and two-photon calcium imaging have been described in detail in a previous study[5].

Animals and two-photon calcium imaging

All experimental procedures were carried out in accordance with institutional animal welfare guidelines and licensed by the Swiss cantonal veterinary office. Mice used in this study were C57Bl/6 wild type mice (3 males, 1 female, Janvier Labs), crosses between Rosa-CAG-LSL-tdTomato (JAX: 007914) and PV-Cre (JAX: 008069) (2 males), and crosses between Rosa-CAG-LSL-tdTomato and VIP-Cre (JAX: 010908) (1 male, 1 female) all obtained from Jackson Laboratory. Mice aged between postnatal days 48-58 were implanted with a chronic imaging window following viral injections of AAV2.1-syn-GCaMP6-WPRE[26]. Imaging began approximately three weeks after surgery using a custom-built resonant scanning two-photon microscope. Images of 750 × 750 pixels and a field of view of 350 µm × 350 µm were acquired with an imaging rate of 32 Hz. We used a piezo Z-scanner (P-726.1CD, Physik Instrumente) to scan 4 planes with 20 µm spacing, resulting in an imaging rate of 8 Hz for each imaging plane. We imaged 8 mice both pre-learning (either first or second day of training) and post-learning (either day 7, 8 or 9 of training). Before each recording session the same imaging site was found by matching anatomical land marks. Mice with bone re-growth under the window, or poor viral expression were excluded from the study.

Behavioral training and discrimination task

Details of the behavioural task have been described in a previous study[5]. Mice were trained in a visual discrimination task as they ran on a styrofoam wheel through a virtual corridor over 9 days. Mice were food deprived to maintain at least 85% of their free-feeding body weight (typically 85-90%). A trial began by displaying black and white circles on the walls of the virtual corridor for a short distance (111 cm), followed by a random distance of gray walls (minimum 74-185 cm, additional random delay chosen from an exponential distribution with mean 37 cm). Mice were then randomly teleported to one of two grating corridors (length 111 cm) with either a vertical grating pattern (square wave gratings, 100% contrast) or an angled grating pattern (rotated 40° relative to vertical) on the walls. Mice were rewarded with a drop of soy milk for licking a reward spout in response to the vertical grating (hits), whereas one or more licks in the angled grating corridor were considered errors (false alarms). We quantified the performance of the mouse using a behavioral d-prime: $bd' = \Phi^{-1}(H) - \Phi^{-1}(F)$, where Φ^{-1} is the normal inverse cumulative distribution function, H is the rate of hit trials and F is the

rate of false alarm trials. Mice were also trained in a similarly structured olfactory discrimination task in the dark where odour 1 (10% soya milk odor) was rewarded and odour 2 (10% soya milk with 0.1% limonene mixture) was not rewarded.

Immunohistochemistry and image registration

Brains were fixed by transcardial perfusion with 4 % paraformaldehyde in phosphate buffer 0.1 M followed by 24 hours of post-fixation in the same solution at 4°C. The whole brains were incubated successively in 20 ml of 10 %, 20 % and 30 % sucrose in phosphate buffer saline (PBS) at 4°C for 1, 8 and 12 hours respectively. For antigen retrieval, the brains underwent two freeze-thaw cycles in liquid nitrogen, followed by three 10 minute washes in PBS. The brains were then sliced tangentially to the surface of visual cortex. 80 µm slices were cut on a vibratome (Zeiss Hydrax V50) and washed three times for 10 minutes each in PBS.

Slices were blocked overnight at room temperature with blocking buffer (Triton X-100 2 %, goat serum 10 %, NaN_3 0.04 % in PBS), incubated in primary antibodies in blocking buffer for twelve hours at room temperature and 2.5 days at 4°C, rinsed three times for one minute and three times for ten minutes in PBS and finally incubated in secondary antibodies in blocking buffer for one day at room temperature. Slices were then rinsed three times for one minute and three times for ten minutes in PBS before being mounted on slides in DABCO-PVA (2.5 % DABCO, 10 % polyvinyl alcohol (Sigma; Type II), 5 % glycerol and 25 mM Tris buffer at pH 8.7). Primary and secondary antibodies were applied in blocking buffer, and are listed in **Supplementary Table 1**.

The slices were imaged with a confocal microscope (Zeiss LSM 700), and confocal z-stacks were compared with the previously acquired in vivo imaging planes and z-stacks of the recording sites[27,28]. We determined the approximate location of the injection site using GCaMP6 fluorescence, and then used blood vessel patterns and cellular morphology to identify the imaging site. We matched at least three points in the confocal z-stack to points in the in vivo imaging plane to obtain a 3-dimensional transformation matrix which was applied to the entire confocal z-stack. Cells were then manually identified and assigned to cell classes based on immunostaining.

To measure the overlap of labelling by transgenic mouse lines and immunostaining, we performed immunostaining on PV, SOM, and VIP transgenic mice (2 mice each) expressing tdTomato in the respective interneuron class, and determined the percentage of overlap between immunostaining and transgenic marker expression, which in each case was above

90% (**Supplementary Table 2a**). We further measured the percentage of transgenically labelled cells that were also identified as belonging to the same interneuron class by immunostaining (**Supplementary Table 2b**). These values give an upper bound on the number of false negatives (interneurons that could not be classified as such due to insufficient immuno-labelling; PV = 7.4%; SOM = 29.9%; VIP = 14.6%). The values for SOM cells may be influenced by the fact that in the SOM-CRE line 6-10% of CRE-positive cells have been reported to be PV interneurons[51].

Simultaneous loose patch and fluorescence measurements

Crosses between PV-Cre (JAX: 008069) and Rosa-CAG-LSL-tdTomato (JAX: 007914) (4 males) were injected with GCaMP6f expressing AAV virus (AAV1.Syn.GCaMP6f.WPRE, vector core, University of Pennsylvania Gene Therapy Program) and VIP-Cre (JAX: 010908, 3 males) or SOM-Cre (JAX: 013044, 3 females) mice were injected with AAV1.Syn.Flex.GCaMP6f.WPRE.SV40, (vector core, University of Pennsylvania Gene Therapy Program) in V1 at P27-P40. After 9-16 days, animals were anesthetized with pentobarbital (150mg/kg), and brains were intracardially perfused by ice cold Choline Chloride solution containing 110 mM Choline chloride, 11.60 mM Na-ascorbate, 7 mM $MgCl_2$, 3.10 mM Na-Pyruvate, 2.5 mM KCl, 1.25 mM NaH_2PO_4, 25 mM $NaHCO_3$, and 25 mM D-Glucose bubbled with a 5% CO_2, 95% O_2 mixture. Coronal slices of cortex (350 µm) were cut in the same Choline chloride solution using a VT1200S vibratome (Leica). After 30 minutes at 32 degrees in ACSF containing 125 mM NaCl, 2.5 mM KCl, 1.25 mM NaH_2PO_4, 26 mM $NaHCO_3$, 2 mM $MgCl_2$, 1 mM $CaCl_2$, 25 mM D-Glucose bubbled with a 5% CO_2, 95% O_2 mixture, slices were brought to room temperature.

Loose patch recordings were performed at 32 degrees in ACSF. Pipettes (5-7 MΩ) filled with 5 mM KCl, 115 mM K-gluconate, 10 mM K-HEPES, 4 mM MgATP, 0.3 mM NaGTP, 10 mM Na-phosphocreatine, 0.1% w/v biocytin were lowered in the bath. Fluorescent cells were targeted for loose-cell patch clamp recordings (seal > 50 MΩ). To induce activity in otherwise quiet slices, a second glass pipette with a potassium-based solution was placed above the recorded cell and slight positive pressure was applied to trigger activity in the recorded neuron. This pipette contained a mixture of internal solution and a diluting solution in 3:7 ratio. The diluting solution contained 150 mM NaCl, 2.5 mM KCl and 10 mM Hepes (final potassium concentration 48 mM). Electrophysiological signals were acquired using a Multiclamp 700B (Axon instruments) filtered between 1 Hz to 2 KHz and digitized at 20 KHz with a NI-PCI6229 (National Instruments) and acquired with WinWCP (John Dempster,

University of Strathclyde). Extracellular spikes were detected using custom Python scripts. Simultaneous two-photon imaging was performed at 34 Hz frame rate using a custom-built two-photon microscope at a wavelength of 940 nm, through a 16× water immersion objective (0.8 NA, Nikon).

Data analysis

Image stacks were corrected for motion and regions of interest (ROIs) were selected for each cell in each session. Raw fluorescence time series F(t) were obtained for each cell by averaging across pixels within each ROI. Baseline fluorescence $F_0(t)$ was computed by smoothing F(t) (causal moving average of 0.375s) and determining for each time point the minimum value in the preceding 600s time window (120s for slice experiments). The change in fluorescence relative to baseline, $\Delta F/F$, was computed by taking the difference between F and F_0, and dividing by F_0. To test the influence of out-of-focus fluorescence from the neuropil surrounding cell body ROIs on neuronal responses of the different cell classes and learning-related changes, we repeated the key analyses after adapting the method of [26] to correct for neuropil contamination of calcium traces (**Supplementary Fig. 12**). We created for each cell a neuropil mask by extending the ROI by 25μm and taking all pixels that were more than 10μm away from the cell boundary, excluding pixels assigned to other cells. In order to avoid including segments of dendrites and axons in the neuropil mask, we computed for each pixel the average fluorescence across all frames, and excluded pixels that were more than 2 standard deviations brighter than the mean across all pixels in the neuropil mask. We performed a robust regression on the relationship between the fluorescence values of the ROI and neuropil mask. By inspecting the slope of this regression in a sample of our dataset we obtained a factor of 0.7 by which we multiplied the neuropil mask fluorescence before subtracting it from the ROI fluorescence.

Responses were analyzed separately for the vertical and angled grating corridor by aligning neuronal activity to the onset of the grating corridors. We used a Wilcoxon rank-sum test to determine if the response of a cell (average $\Delta F/F$ in a time window of 0-1 s after grating onset) was significantly different for vertical and angled gratings ($P < 0.05$). Within stimulus conditions, we used a Wilcoxon signed-rank test to determine if the response ($\Delta F/F$ 0-1 s) to the gratings significantly increased or decreased relative to baseline (-0.5 to 0 s). For visualizing stimulus-evoked responses (**Fig. 1e, Supplementary Fig. 2a, b, 3, 4b, e**), and for computing the change in stimulus-evoked responses with learning (**Supplementary Fig. 4c,**

f), we subtracted the pre-stimulus baseline (-0.5 to 0 s before stimulus onset) from the average response.

We quantified the selectivity of each cell as the selectivity index (SI) which was the difference between the mean response (0-1 s) to the vertical and angled grating divided by the pooled standard deviation. The selectivity was positive for cells that preferred the vertical grating and negative for cells that preferred the angled grating. To determine the significance of changes in the SI with learning of single cells (**Fig. 2c**), we used a bootstrap procedure. We randomly selected for every pre-learning session trials with replacement 1000 times and compute the SI to obtain the 2.5 and 97.5 percentiles of the pre-learning selectivity. An increase or decrease in the SI was considered significant if the post learning selectivity was outside this interval. To obtain an average measure of the selectivity across a population of cells including vertical and angled preferring cells, we took the average of the absolute selectivity of all cells (**Fig. 2d, Supplementary Fig. 5e-j, 12a**). We calculated the selectivity of the local PYR population around each interneuron by averaging the responses of all PYR cells within 100 μm distance, to the two grating stimuli (**Fig. 2g, h, Supplementary Fig. 12b**). We calculated the confidence intervals for the slope in these figures by a bootstrap procedure where we randomly selected cells with replacement 10,000 times to obtain the 2.5 and 97.5 percentiles. The P value was given by the percentage of bootstrapped pre-learning slope values that were lower than the post-learning slope multiplied by two (two-sided test). To compute Δselectivity, we subtracted the absolute selectivity with weights intact from the absolute selectivity with weights deleted (**Fig. 4e-i**), or we subtracted the absolute selectivity before learning from the absolute selectivity after learning (**Fig. 5b, c**).

We used the Pearson correlation coefficient to quantify the correlation between responses of pairs of cells. The significance of the correlation coefficient was determined using Student's t-distribution. Noise correlation was computed by first subtracting for each trial and each cell the average responses across all trials. Changes in noise correlations with learning between different cell types (**Fig. 3c)** were tested using a sign test with Bonferroni correction on all cells imaged pre- and post-learning. Noise correlation with a population (population coupling, **Fig. 5**) was computed by averaging the activity of all cells belonging to a specific cell class in a given recording (the population activity) and calculating the noise correlation of an individual cell with this population activity of a given cell class as above. Correlations from the two grating stimulus conditions were averaged. To establish that the difference in Δselectivity of PYR cells that strongly or weakly correlated with the SOM population (**Fig. 5b**) was not due to any differences in the selectivity of the selected cells pre learning, we

repeated the analysis including only cells that were non-selective pre learning (N = 152 cells in each group). Cells were classified as non-selective if their responses to the two grating stimuli in a time window of 1s after grating onset were not significantly different (Wilcoxon rank-sum test, $P > 0.05$).

We quantified differences between response profiles across cell classes by using a random forest decoder that classified cells to one of two classes based on the shape of the baseline-subtracted response, averaged across all trials (**Fig. 1g**, **Supplementary Fig. 2d**). For a given pair of cell classes, we randomly picked 20 cells of each class to train the decoder (Matlab function TreeBagger, with parameters $N_{trees} = 32$, minleaf = 5), and estimated the accuracy of classifying the cells of each class that were not used for training. We repeated this procedure 1000 times for each pair of cell classes and averaged the accuracies to obtain the classification accuracy. In order to estimate the baseline classification accuracy, we randomly picked two sets of 20 cells from the same class to train the decoder. We used the classification accuracy (CA) to compute the similarity score $SS = 2 \cdot (1 - CA)$, where scores near 0 and 1 indicate low and high response profile similarity between two cell classes respectively.

We controlled for the possible effect of variations across learning in running speed, eye position, pupil radius, and occurrences of eye movements and licking on selectivity and correlations, by using a stratification approach[5]. We selected a subset of trials with similar distributions of eye position, pupil radius or running speed before and after learning. We then recomputed the selectivity and noise correlations before and after learning and obtained similar results with and without stratification (**Supplementary Figs. 5d, e, h, 8a, b, e**). We also used a stratification approach to determine whether the reduction in noise correlation could be explained by a reduction in response strength with learning. For every cell pair where one (or both) of the two cells showed a significant decrease in response strength with learning, we selected a subset of trials with similar distribution(s) of response strength before and after learning. After recomputing the noise correlations, we observed similar results (**Supplementary Fig. 8f**). Before learning, mice licked with a mean latency of 3.14 s (median 1.06 s) and after learning the mean lick latency was 2.32 s (median 1.59 s) relative to stimulus onset. Therefore, in most trials mice licked only after the analysis window. Furthermore, on excluding trials with licks or eye movements in the analysis window we obtained similar results (**Supplementary Figs. 5f, g, 8c, d**). To determine the contribution of variations in running speed and eye position to the strength of noise correlations, we compared noise correlations computed on a subset of trials with reduced variability to noise correlations

computed on a random subset. More specifically, for every post learning session we computed the average running speed for each trial (0-1 s after grating onset). We then picked trials from the middle 50% of this distribution (25th to 75th percentile) and picked an equal number of trials sampled randomly from the full distribution. We repeated the random selection 10 times and took the average noise correlations. Noise correlations obtained for the middle 50% and random selection were very similar, both for individual cells (**Supplementary Fig. 9a**), and for the average noise correlations between specific cell classes (**Supplementary Fig. 9b**). We also performed a similar analysis for the horizontal eye position after computing the average eye position for each trial (0-1 s after grating onset) (**Supplementary Fig. 9c, d**). The task-irrelevant patterns of white and black circles on the walls at the beginning of the approach corridor evoke robust and selective neural responses (see Poort et al., Neuron 2015, Figure S7). As described previously, we computed the selectivity of responses by comparing the response strength at different corridor locations (the length of the corridor section with black and white circles was 111 cm, divided into 60 position bins). More specifically, selectivity was calculated as the standard deviation of the mean response across positions S_R divided by the pooled standard deviation across positions: $(2 \cdot S_R)/S_p^{pos}$, where $S_p^{pos} = \sum_{i=1}^{k=N_{pos}}(n_i - 1)s_i^2 / \sum_{i=1}^{k}(n_i - 1)$ and N_{pos} is the number of position bins[5].

We performed statistical tests which included information about the nesting of cells within animals with a linear mixed-effects model (Matlab function fitlme). The analysis in **Fig. 2d** was repeated using a linear mixed-effects model with a fixed effect for learning stage and a random effect for cell identity (nested within animals), which returned similar results to those reported above (P-values for PYR, PV, SOM and VIP cells respectively: $P < 10^{-16}$, $P < 10^{-6}$, P = 0.023, P = 0.92). We also repeated the same analysis after controlling for eye position, pupil size, eye movements, running and licking (**Supplementary Fig. 5b-i**) using a linear mixed-effects model with a fixed effect for learning stage and a random effect for cell identity (nested within animals), which returned similar results to those reported (P-values for PYR, PV, SOM and VIP cells respectively: $P < 10^{-15}$, $P < 10^{-6}$, P = 0.002, P = 0.04 (eye position), $P < 10^{-7}$, $P < 10^{-4}$, P = 0.40, P = 0.002 (pupil size), $P < 10^{-14}$, $P < 10^{-4}$, P = 0.25, P = 0.30 (eye movements), $P < 10^{-10}$, $P < 10^{-4}$, P = 0.003, P = 0.26 (running speed), $P < 10^{-5}$, $P < 10^{-5}$, P = 0.08, P = 0.03 (licking). We also repeated the analysis in **Supplementary Fig. 5j** using a linear mixed-effects model with a fixed effect for learning stage and a random effect for cell identity (nested within animals), which returned similar P-values for PYR, PV, SOM and VIP cells respectively: $P < 10^{-16}$, P = 0.002, P = 0.009, P = 0.007). The analysis in **Fig. 2g, h** was

repeated with a linear mixed-effects model with the selectivity of PV or SOM as fixed effect and cell identity (nested within animals) as random effect, which also returned similar results and confidence intervals as those reported above (PV, slope before learning 0.20, CI 0.14 to 0.26, after learning 0.05, CI 0.02 to 0.09, SOM slope before learning 0.14, CI 0.05 to 0.23, after learning 0.15, CI 0.08 to 0.22). The analysis in **Fig. 3c** was repeated using the linear mixed-effects model with a fixed effect for learning stage and a random effect for cell identity (nested within animals) also resulting in similar P-values (all Ps < 10-4, with the exception of SOM-SOM cell pairs, P = 0.87). Finally, the analysis in **Fig. 5** was repeated using the linear mixed-effects model with a fixed effect for correlation category and a random effect for animal identity also resulting in similar P-values (all Ps > 0.05, with the exception of pre-learning PYR-SOM coupling, $P < 10^{-3}$).

Linear Multivariate Autoregressive System Model

We modeled the activity of the simultaneously imaged neurons using a multivariate autoregressive (MVAR) linear dynamical system incorporating stimulus-related input. The MVAR model takes advantage of the simultaneously measured co-fluctuations from multiple cells of different cell types before and after learning to estimate the interaction weights between pairs of cells. The interaction weights describe the relationship between the activity of one cell and the activity of another cell at previous timepoints, conditioned over the activity of all other cells and over behavioral and sensory variability, thereby being more causal in nature and going beyond measures such as simple correlation. For each imaging session, we extracted the ΔF/F signals from all N_{neuron} neurons in N trials, each spanning -1 to 1 s (in timesteps $t = 0 \ldots T$) relative to the onset of a grating stimulus (stimulus label $s = 1, 2$ for vertical and angled gratings respectively) or to the onset of the gray pre-stimulus period ($s = 0$), and collected the measured activity of all neurons in the population at time sample t of trial i into a vector $\mathbf{r}_t^{(i)}$. The change in this vector at time t was modeled as depending linearly on the preceding population activity vector through an interaction matrix A, on the stimulus through a time-dependent input vector $\mathbf{u}_t^{(s)}$ (common to all trials with the same stimulus), and on the instantaneous running speed of the animal $v_t^{(i)}$ through a weight vector $\boldsymbol{\xi}$. This gave the model:

$$\mathbf{r}_t^{(i)} = \mathbf{r}_{t-1}^{(i)} + A\mathbf{r}_{t-1}^{(i)} + \mathbf{u}_t^{(s)} + \boldsymbol{\xi} v_t^{(i)} + \mathbf{e}_t^{(i)} \quad (1)$$

where $\mathbf{e}_t^{(i)}$ represents a residual term capturing the activity unexplained by the other factors. We fit the parameters A, $\mathbf{u}_t^{(s)}$ (for $s = 0, 1, 2$ and all times t in the trial), and $\boldsymbol{\xi}$ by minimizing the sum of squared residuals over all trials i and time samples t. Model fitting was blind to cell type.

The least-squares fit parameters could be found analytically, and the corresponding forms are instructive regarding the relationship between parameters and properties of the data. For simplicity we neglect the velocity-related term in the following equations. Let $\boldsymbol{\mu}_t^{(s)}$ be the average population activity vector at time sample t on trials where stimulus s was presented: $\boldsymbol{\mu}_t^{(s)} = \frac{1}{N^{(s)}} \sum_{i:\mathrm{stim}(i)=s} \mathbf{r}_t^{(i)}$, where the sum is over trials with stimulus s and $N^{(s)}$ is the number of such trials. We define sample covariance matrices $\Sigma_0^{(s)} = \frac{1}{TN^{(s)}} \sum_{t=0}^{T-1} \sum_{i:\mathrm{stim}(i)=s} \left(\mathbf{r}_t^{(i)} - \boldsymbol{\mu}_t^{(s)}\right)\left(\mathbf{r}_t^{(i)} - \boldsymbol{\mu}_t^{(s)}\right)^T$ and $\Sigma_{+1}^{(s)} = \frac{1}{TN^{(s)}} \sum_{t=0}^{T-1} \sum_{i:\mathrm{stim}(i)=s} \left(\mathbf{r}_{t+1}^{(i)} - \boldsymbol{\mu}_{t+1}^{(s)}\right)\left(\mathbf{r}_t^{(i)} - \boldsymbol{\mu}_t^{(s)}\right)^T$. Then the parameter estimates are:

$$\hat{A} = \left(\sum_{s=0}^{2} N^{(s)} \Sigma_{+1}^{(s)}\right)\left(\sum_{s=0}^{2} N^{(s)} \Sigma_0^{(s)}\right)^{-1} - \mathbb{I} \qquad (2)$$

$$\hat{\mathbf{u}}_t^{(s)} = \boldsymbol{\mu}_t^{(s)} - (\hat{A} + \mathbb{I})\, \boldsymbol{\mu}_{t-1}^{(s)} \qquad (3)$$

$$\mathbf{e}_t^{(i)} = \left(\mathbf{r}_t^{(i)} - \boldsymbol{\mu}_t^{(s)}\right) - (\hat{A} + \mathbb{I})\left(\mathbf{r}_{t-1}^{(i)} - \boldsymbol{\mu}_{t-1}^{(s)}\right) \qquad (\text{for } \mathrm{stim}(s) = i), \qquad (4)$$

where $\mathbb{I}$ is the identity matrix. Equation (2) shows that the interaction weights are fully determined by the sample covariance of the data, and independent of the mean profile. Conversely, given this matrix, the stimulus-related inputs depend only on the mean response profile (Equation 3). Finally, Equation (4) indicates that the residuals $\mathbf{e}_t^{(i)}$ capture the deviation from the mean profile that remains unexplained by the estimated interaction matrix and the measured initial state $\mathbf{r}_0^{(i)}$.

In practice, we fit the MVAR model using a numerical linear system solver (*mrdivide* in MATLAB, Mathworks, Natick MA) applied to the single matrix equation $\Delta R = \Lambda\Gamma$, where: ΔR is the $N_{\mathrm{neuron}} \times TN$ matrix formed by horizontally concatenating the changes $\mathbf{r}_t^{(i)} - \mathbf{r}_{t-1}^{(i)}$ for times $t = 1 \ldots T$ over all trials; Γ is the $(N_{\mathrm{neuron}} + 3NT + 1) \times NT$ matrix formed by vertically concatenating matrices $R, J^{(0)}, J^{(1)}, J^{(2)}$ and V, with R formed from the measured responses $\mathbf{r}_t^{(i)}$ for $t = 0 \ldots T-1$ over all trials, $J^{(s)}$ containing a $T \times T$ identity matrix for each trial with stimulus s and 0s elsewhere, and V formed from the running speeds $v_t^{(i)}$ for

times $t = 1 \ldots T$ over all trials; and finally Λ concatenates the parameters to be estimated: $\Lambda = \left[A, \mathbf{u}_1^{(0)}, \ldots, \mathbf{u}_T^{(0)}, \mathbf{u}_1^{(1)}, \ldots, \mathbf{u}_T^{(1)}, \mathbf{u}_1^{(2)}, \ldots, \mathbf{u}_T^{(2)}, \boldsymbol{\xi}\right]$. We first fit separate models using either the pre- or post-learning data for each individual mouse. We then modeled pre- and post-learning data jointly, while constraining a subset of the parameters to remain fixed (**Supplementary Fig. 11e**). Specifically, for each mouse we concatenated pre- and post-learning trials to form the matrix $\Delta R = \left[\Delta R_{\mathrm{pre}}, \Delta R_{\mathrm{post}}\right]$. The construction of Γ then determined which parameters were held fixed over learning. When $\Gamma = \left[R_{\mathrm{pre}}, 0; 0, R_{\mathrm{post}}; J_{\mathrm{pre}}, 0; 0, J_{\mathrm{post}}; V_{\mathrm{pre}}, 0; 0, V_{\mathrm{post}}\right]$ (with semicolons representing vertical concatenation and $J = \left[J^{(0)}; J^{(1)}; J^{(2)}\right]$) no parameters are constrained and this method becomes equivalent to fitting the model separately pre- and post-learning. When $\Gamma = \left[R_{\mathrm{pre}}, R_{\mathrm{post}}; J_{\mathrm{pre}}, J_{\mathrm{post}}; V_{\mathrm{pre}}, V_{\mathrm{post}}\right]$, all parameters are constrained and this method becomes equivalent to fitting a single model to capture activity both before and after learning. Partial constraints fall between these extremes. For example, to fix all interaction weights over learning while allowing all stimulus-related inputs to change, we set $\Gamma = \left[R_{\mathrm{pre}}, R_{\mathrm{post}}; J_{\mathrm{pre}}, 0; 0, J_{\mathrm{post}}; V_{\mathrm{pre}}, V_{\mathrm{post}}\right]$ whereas to allow interactions to change while keeping stimulus-related inputs fixed we set $\Gamma = \left[R_{\mathrm{pre}}, 0; 0, R_{\mathrm{post}}; J_{\mathrm{pre}}, J_{\mathrm{post}}; V_{\mathrm{pre}}, V_{\mathrm{post}}\right]$. In all such models, we held the velocity modulation coefficients fixed over learning.

We tested the performance of the MVAR model using leave-one-out cross validation (**Supplementary Fig. 10b, c**), measuring prediction quality on held-out data. We held out one vertical grating trial in the test set, using the remaining trials of all types for training. The MVAR model was fit to these training data, and the error in the model prediction was calculated for each time sample in the test trial. This procedure was repeated $N^{(1)}$ times, leaving out each vertical grating trial in turn. An R^2 value for each cell was then calculated combining errors across all of these trials. To ease comparison with alternative models, running speed was not included in the model for the cross-validation analysis.

We benchmarked the MVAR model against three alternative models using this cross-validation method. In the response profile only model, the predicted activity of each cell was given by its average response profile over the training data for the vertical grating stimulus. This is equivalent to an MVAR model with all elements of the interaction matrix set to zero. The second alternative was equivalent to the MVAR model with off-diagonal elements of the interaction weight matrix set to zero. This model therefore incorporates autocorrelations and fluctuations in baseline from trial to trial, but not any additional cross-correlations between

cells. This model was fit by subtracting the average response profile from each cell, and then regressing the resulting signal for each cell against its own activity at the previous time step, to obtain a single regression weight for each cell. The third model was equivalent to the MVAR model with interaction weights that vary with time relative to stimulus onset. To fit this model, we subtracted the average response profile and regressed the activity of the population against the activity of the population at the previous time step. This regression was done separately for each time sample relative to stimulus onset to obtain a full interaction weight matrix for each time sample.

To analyze the contribution of neuronal interactions and stimulus-related inputs to the measured responses we derived analytical expressions for the responses produced by the model under a given set of parameters:

$$\mathbf{r}_t^{(i)} = (A + \mathbb{I})^{\mathrm{t}}\mathbf{r}_0^{(i)} + \sum_{\tau=1}^{t}(A + \mathbb{I})^{\mathrm{t}-\tau}\left(\mathbf{u}_\tau^{(s)} + \boldsymbol{\xi} v_\tau^{(i)} + \mathbf{e}_\tau^{(i)}\right) \quad (5)$$

Using this equation, we computed the population responses when weights were deleted (set to zero) and when residuals were shuffled (**Fig. 4c, d**). In the model, the interaction weights are a function of only the covariance of the data (see Equation 2) and the residuals contain any variability not captured by the model.

We derived analytical expressions for the covariance between cells generated by the model. For simplicity, we omitted the running speed term and assumed that residuals were stationary and lacked intertemporal covariance, and that residuals did not covary with the initial state, i.e., $\langle \mathbf{e}_t \mathbf{e}_{t-\tau} \rangle = \delta_{t,t-\tau}\, \Sigma_{\mathbf{e}}$ and $\langle \mathbf{e}_t \mathbf{r}_0^T \rangle = 0$ where angle brackets represent expectations over trials, $\delta_{t,t'}$ is the Kronecker delta, and $\Sigma_{\mathbf{e}}$ is the covariance matrix of the residuals. Then from Equation (5) it follows that the response covariance between cells at time t is given by

$$\Sigma_{\mathbf{r}_t} = (A + \mathbb{I})^{\mathrm{t}}\Sigma_{\mathbf{r}_0}(A^T + \mathbb{I})^{\mathrm{t}} + \sum_{\tau=1}^{t}(A + \mathbb{I})^{t-\tau}\Sigma_{\mathbf{e}}(A^T + \mathbb{I})^{t-\tau} \quad (6)$$

From this expression it can be seen that covariance between the responses of cells can only be generated by off-diagonal elements of $\Sigma_{\mathbf{r}_0}$, A, or $\Sigma_{\mathbf{e}}$. By shuffling residuals, we remove off-diagonal elements of $\Sigma_{\mathbf{e}}$. By deleting weights between cells, we remove off-diagonal elements of A. Thus, the degree to which the observed covariance was accounted for by correlations in the residuals was assessed by simulating the responses after shuffling the residuals. To determine the degree to which the observed covariance was accounted for by interaction weights, we simulated responses after deleting the interaction weights. These manipulations allowed us to test whether the model captured the coordinated variability in the data using a

set of parameters fixed across trials, without requiring any additional unexplained inputs that covary across trials or time.

To shuffle residuals in **Fig. 4c, d**, we randomly permuted the trial labels of the residuals across all vertical stimulus trials separately for each cell and then computed the responses according to Equation (2) by substituting the shuffled residuals. Having calculated the responses under residual shuffling, we then computed pairwise noise correlations using the same method as for the experimental data. We repeated this for 100 random shuffles and averaged over the noise correlations generated by these shuffles for each cell pair. To calculate the noise correlations when interactions are removed (**Fig. 4c, d**), we set all off-diagonal elements of the interaction matrix A to zero and then computed the responses according to Equation (2). We again calculated the noise correlations of these responses as above. To quantify the quality of the fit after shuffling residuals and removing interactions we computed R^2 of the noise correlations of the data compared to model under the relevant manipulation.

To compute the selectivity of responses following weight deletions we set either all or specific off-diagonal weights of a given type to zero (leaving diagonal elements of the weight matrix intact), calculated responses as above, and averaged responses for each cell to the vertical and angled stimulus similar to the experimental data. Because the interaction weights in the MVAR model organize to best capture the variance in the data (see above), deleting weights removes the majority of simulated response variance. We therefore used the measured variance to calculate selectivity after weight deletions. To determine whether the effect of weight deletion changed with learning, we computed both pre- and post-learning, the selectivity index with all weights intact, SI full, and the selectivity with specific weights deleted, $\mathrm{SI}_{\mathrm{del}}$, and then compared $\left|\mathrm{SI}_{\mathrm{del,pre}}\right| - \left|\mathrm{SI}_{\mathrm{full,pre}}\right|$ to $\left|\mathrm{SI}_{\mathrm{del,post}}\right| - \left|\mathrm{SI}_{\mathrm{full,post}}\right|$ using a sign test.

To test whether interaction weights identified by the model were dependent on the stimulus-related input preference of the cell (**Fig. 4j, Supplementary Fig. 11c, d**), we separated cell pairs into groups according to the mean stimulus-related input they received in the 0 to 1 s window from stimulus onset at the vertical and angled gratings. If both cells in the pair had a larger stimulus-related input for the same grating, they were considered to have the same grating preference (either to the vertical or angled stimulus), otherwise they were considered to have opposite preferences. We measured the mean interaction weight between cell pairs that preferred the same or different gratings. Only cells whose responses were significantly

different to the vertical and angled gratings were included in the analysis (criterion P < 0.05, Wilcoxon rank-sum test).

To test how well the changes in selectivity were captured by the model with a given set of parameters fixed, we shuffled the trial labels of the residuals across the combined set of pre- and post-learning trials which removed any response changes not captured by the model (leaving the residuals across cells and time within a given trial intact). We then recomputed the responses using Equation (2) by substituting the shuffled residuals, and computed the selectivity of these responses pre- and post-learning. We repeated this process for 100 random shuffles and averaged the resulting selectivity over shuffles. We then computed the R^2 value of the model-generated change in selectivity vs the change in selectivity observed in the data. To generate confidence intervals for these R^2 values we performed a bootstrap over cells.

To perform hypothesis testing that two models (Model 1 and Model 2) generated R^2 values that differed more than would be expected by chance, we performed a model-based bootstrap (see legend of **Supplementary Fig.11c**). For the model-based bootstrap, we first fit the data to Model 1. We then generated a new dataset from Model 1 by randomly resampling residuals (with replacement) and computing responses according to Equation (2). Next, we fit Models 1 and 2 to the dataset generated from Model 1, and computed the R^2 of the change in selectivity generated by these models against the change in selectivity in the simulated dataset from Model 1. We repeated this process 500 times to obtain a distribution of the difference in R^2 between Model 1 and Model 2 that would be expected if the data were generated by Model 1.

Statistics

Data are reported as mean ± SEM or as mean ± STD as indicated. All data analyses were performed using custom code written in Matlab. No assumptions of normality of data distributions were imposed. The non-parametric Wilcoxon rank-sum test and sign test were used to study differences between two groups of unpaired and paired data respectively. Bonferroni correction was applied for multiple comparisons as indicated. No test for equal variance was performed. Bootstrap tests were performed as indicated. Multilevel analysis was performed in some cases to account for nested experimental design. No statistical methods were used to pre-determine sample sizes, but our sample sizes are similar to those in prior reports and are typical for the field. All statistical tests were two-sided, and *P*-values <0.05 were considered statistically significant. No randomization or blinding was performed during experiments or data analysis.

Life Sciences Reporting Summary

Further information on experimental design is available in the Life Sciences Reporting Summary.

Data and code availability

The data and code that support the findings of this study are available from the corresponding authors upon reasonable request.

Methods References

51. Hu, H., Cavendish, J. Z. & Agmon, A. Not all that glitters is gold: off-target recombination in the somatostatin-IRES-Cre mouse line labels a subset of fast-spiking interneurons. *Front. Neural Circuits* **7,** 195 (2013).

Figures

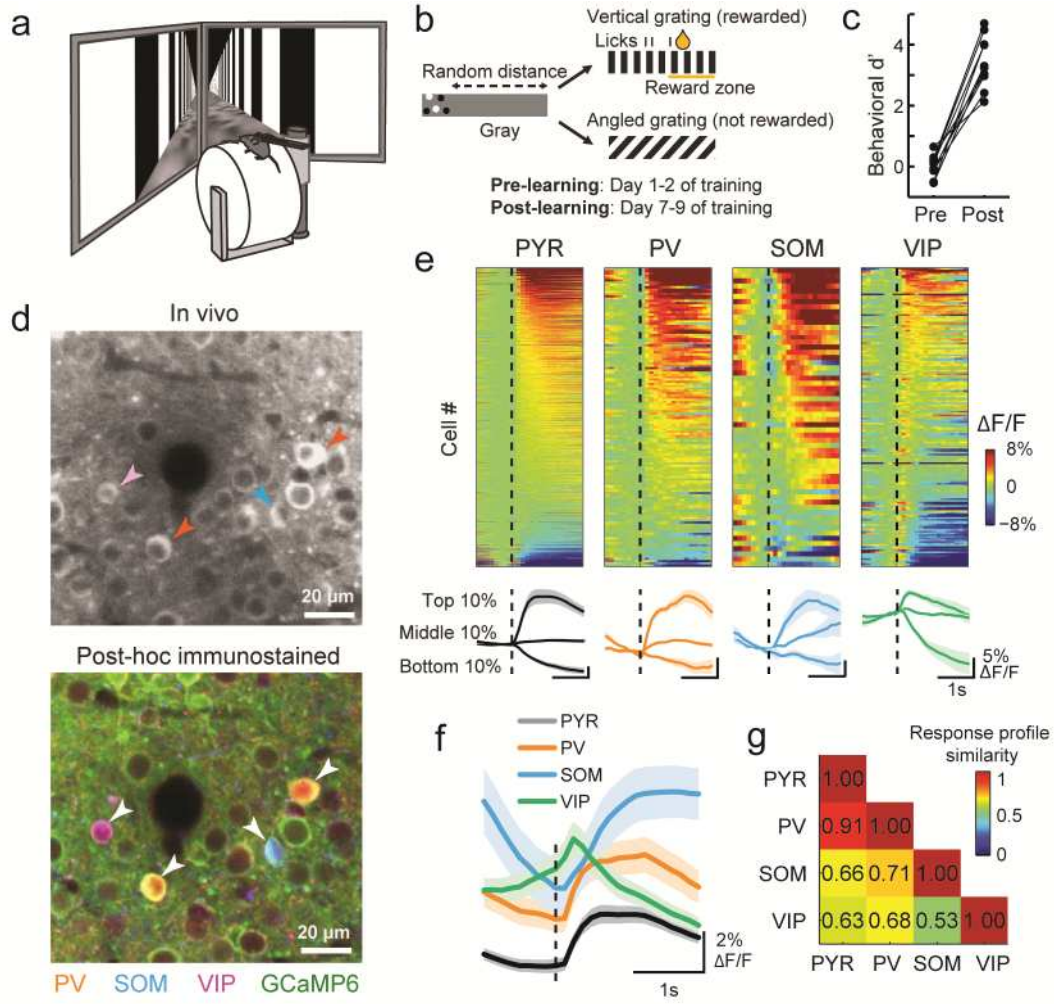

Figure 1. Simultaneous two-photon imaging of multiple cell classes during a visual discrimination task in virtual reality. (**a**) Virtual reality setup. (**b**) Schematic of behavioral task. Mice were rewarded for licking a reward spout when presented with vertical and not angled gratings. (**c**) Behavioral discrimination performance (behavioral d') across learning (N = 8 mice). Connected points represent individual mice. (**d**) Top, example region of an in-vivo image plane with GCaMP6f expressing neurons. Bottom, same region after post-hoc immunostaining for PV, SOM and VIP (orange, blue and magenta, respectively) and image registration to match the in-vivo plane. Identified interneurons are indicated by arrowheads. Image registration and cell matching was performed for each mouse (N=8) (**e**) Top, average responses to the vertical grating of all recorded neurons of each cell type after learning. Calcium responses are baseline corrected (subtraction of baseline ΔF/F -0.5 to 0 s before stimulus onset), and aligned to grating onset (dashed line). Cells are sorted by their average response amplitude 0-1 s from stimulus onset. Number of cells included in each plot: 1249, 132, 58 and 175 for PYR, PV, SOM and VIP, respectively, N = 8 mice. Bottom, average responses of cells from the top, middle and bottom 10th percentiles of grating-evoked response amplitudes of each cell class (125, 13, 6 and 18 cells in each 10th percentile, respectively). Shaded area represents SEM. (**f**) Average response to the vertical grating of all cells from each cell class after learning. (**g**) Similarity of response profiles to the vertical grating of all pairs of cell classes attained with a random forest decoder to classify single cells to one of two classes based on the shape of their average baseline-subtracted response profiles (see Online Methods). Response profile similarity score = 2 × (1- classification accuracy).

Scores near 0 and 1 indicate low and high response profile similarity between two cell classes respectively.

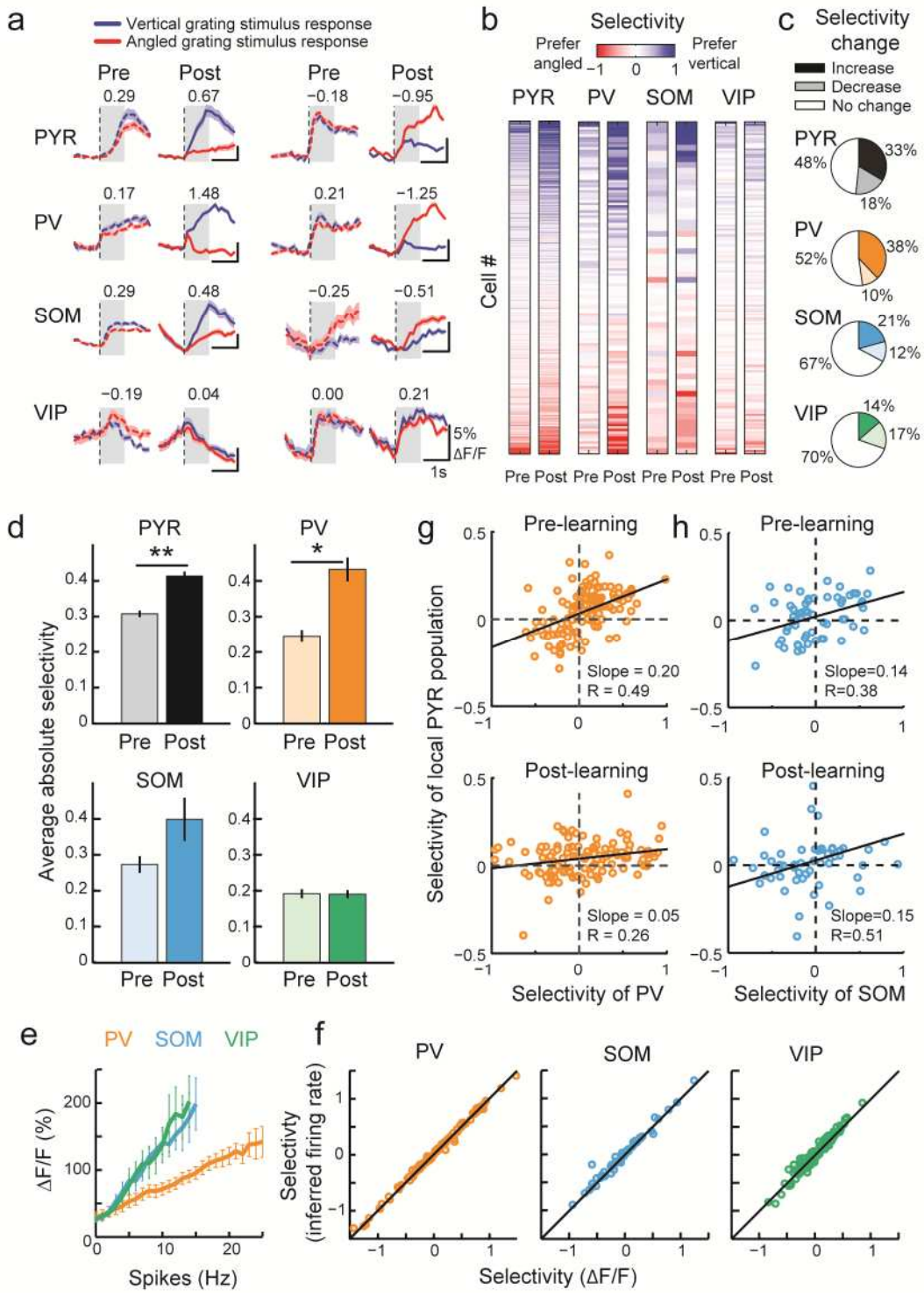

Figure 2. Response amplitude and stimulus selectivity changes with learning in different cell classes. (**a**) Average responses to vertical (blue line) and angled (red line) grating stimuli before (dashed line) and after learning (solid line) of example neurons from different cell classes. Numbers indicate selectivity to the grating stimuli, calculated in a window 0-1s from grating stimulus onset (gray shading). Positive and negative values indicate vertical and angled preference, respectively. Shaded area represents SEM. (**b**) Grating selectivity of the same cells (rows) before (pre) and after (post) learning (columns). Cells were ordered by their

mean pre- and post-learning selectivity. Numbers of cells recorded both pre- and post-learning: 1249 PYR, 132 PV, 58 SOM and 175 VIP cells here and in c,d,f,g and h, N = 8 mice. (**c**) Percentage of cells in each cell class which displayed a significant increase, decrease or no change in selectivity during learning (bootstrap test, $P < 0.05$). (**d**) Mean absolute selectivity of each cell class before and after learning. Error bars represent SEM here and elsewhere. Sign test, **, $P < 0.001$; *, $P < 0.05$ (PYR, $P < 10^{-7}$; PV, $P = 0.002$; SOM, $P=0.51$; VIP, $P=1$). Data distribution shown in **Supplementary Fig. 5a**. (**e**) Relationship between action potential firing rate and calcium transient size in simultaneous loose patch and GCaMP6f recordings from the three interneuron classes in visual cortex slices (13 PV, 17 SOM and 11 VIP cells). (**f**) Comparison of selectivity values computed from measured fluorescence (x-axis) and inferred firing rate (y-axis) in PV, SOM, and VIP interneurons. Pearson correlation coefficients 1.00, 0.99, 0.97 for PV, SOM and VIP respectively (**g, h**) Relationship between the selectivity of individual PV cells (**g**) or SOM cells (**h**) and the mean selectivity of the local PYR population within 100 μm distance from each PV or SOM cell, before (top) and after learning (bottom). Exact P values are reported only for $P > 0.001$.

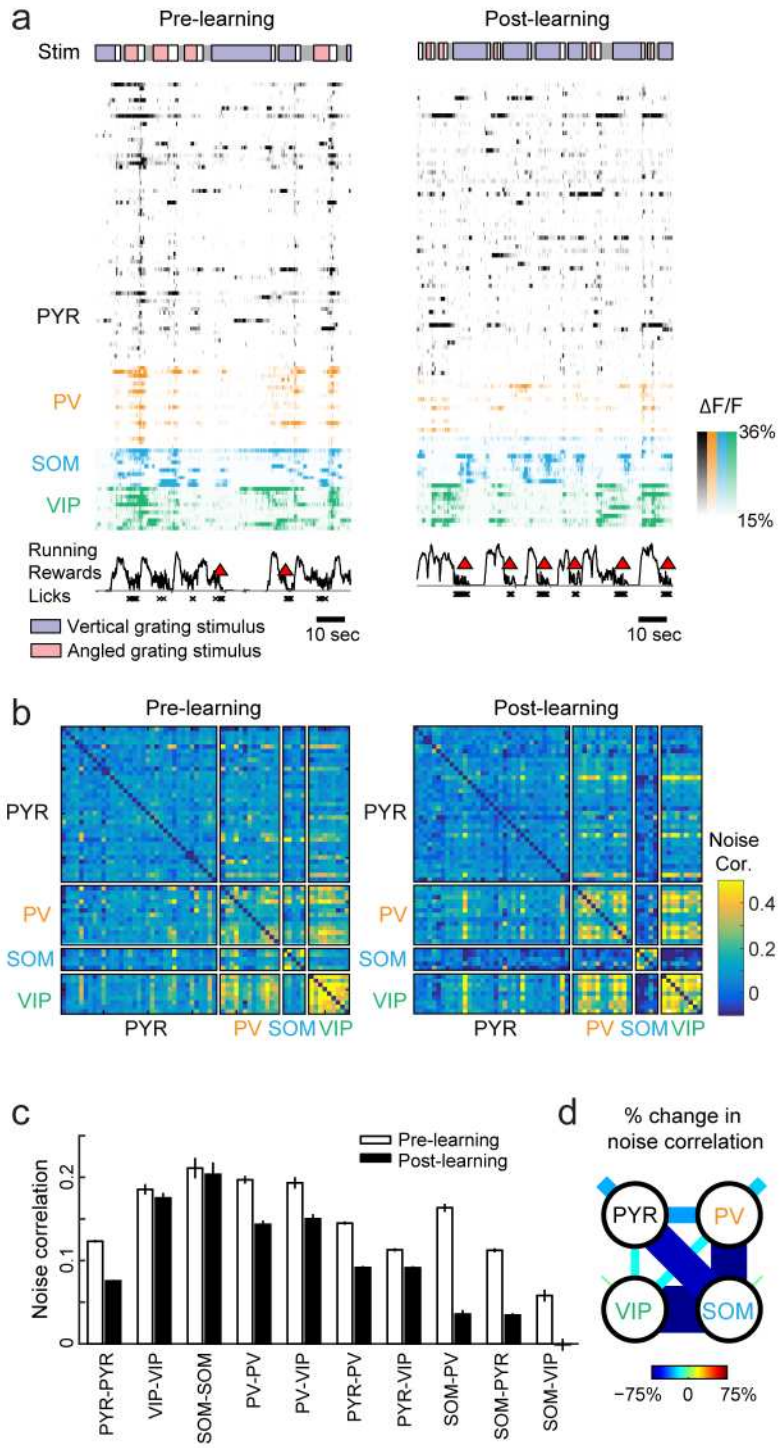

Figure 3. Changes in neuronal co-fluctuations with learning. (**a**) Example responses of simultaneously imaged neurons before (left) and after learning (right). Colored bars on top indicate stimuli encountered by the mouse as it traversed the virtual corridor: blue and red indicate vertical and angled gratings, gray and white indicate corridor walls in gray or with dots, respectively. Running (black line), reward delivery (red triangle) and licks (crosses) are indicated below. (**b**) Example matrices of noise correlations measured during the vertical grating response (0-1 s from stimulus onset) between cell pairs of the same neurons imaged before (left) and after learning (right). Only a quarter of the recorded PYR cells are shown in **a** and **b** for clarity. (**c**) Average noise correlations between cell pairs for each combination of cell classes, before and after learning. Only cells with significant responses to the grating stimuli were included. The number of cell pairs in each cell class combination (pre, post-

learning) was: PYR-PYR 77599, 66633, VIP-VIP 984, 776, SOM-SOM 201, 131, PV-PV 1646, 1316, PV-VIP 818, 702, PV-PYR 17496, 15029, PYR-VIP 14485, 11893, SOM-PV 1176, 828, SOM-PYR 7121, 5545, SOM-VIP 476, 364. Error bars represent SEM. Full data distribution can be seen in **Supplementary Fig. 7b**. (**d)** Relative changes in noise correlation (shown in **c**) over learning between and within all cell classes, as indicated by line thickness and color code. Shorter line segments show relative change in correlations between cells of the same type.

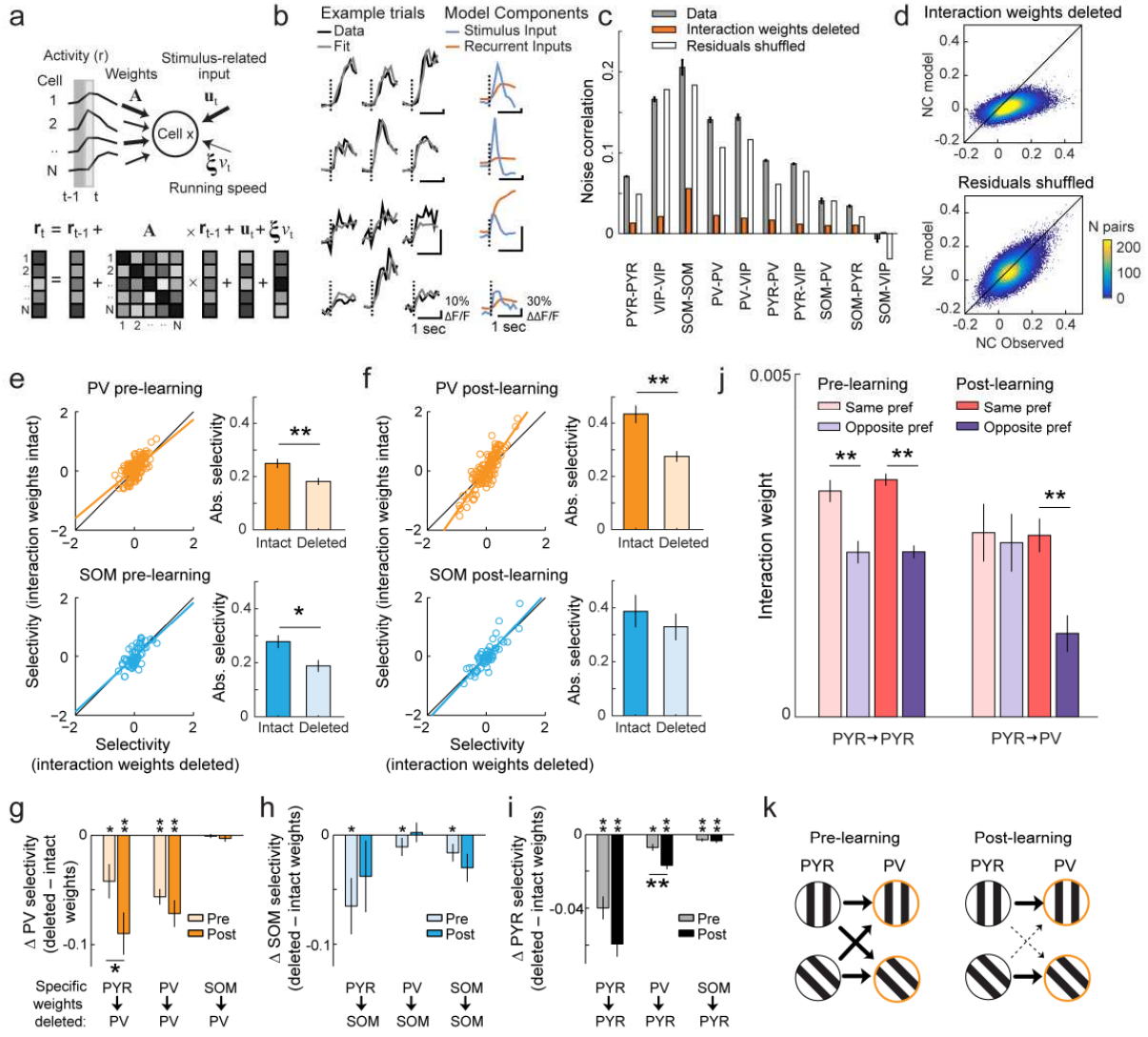

Figure 4. A multivariate autoregressive (MVAR) linear dynamical system model indicates emergence of specific PYR-PV interactions with learning. (**a**) An MVAR model fits single trial responses by estimating the contribution of stimulus-locked input, recurrent inputs from the local cell population and running speed. (**b**) Example traces of responses and model fit on three single trials (columns) from 4 cells (rows) along with each cell's stimulus input (blue) and average recurrent input (red). (**c**) Average post-learning noise correlations between all cell pairs, observed (gray), or simulated after deleting interaction weights (orange) or shuffling residuals (white). Error bars represent SEM here and below. (**d**) Scatter density plot of observed versus simulated pairwise noise correlations (NC), after deleting interaction weights or shuffling residuals. N = 103217 cell pairs. (**e, f**) Effect on selectivity of deleting all interaction weights in the MVAR model onto PV (top) or SOM cells (bottom) before (**e**) and after (**f**) learning. Bars indicate average absolute selectivity with weights intact and deleted. Sign test, **, $P < 10^{-3}$; *, $P < 0.05$ here and below. N = 1249 PYR, 132 PV and 58 SOM cells

here and below. (**g, h, i**) Effect of deleting specific interaction weights (Δselectivity) onto PV (**g**), SOM (**h**) and PYR cells (**i**) on their selectivity pre- and post-learning. * with horizontal line indicates pre-post learning comparison, * at base of bar indicates significant difference between intact and deleted weights, pre- or post-learning. Data distribution shown in **Supplementary Fig. 11b**. (**j**) Interaction weights in MVAR model before and after learning for cell pairs with the same or opposite stimulus-input preference. N interaction weights pre- and post-learning for same or opposite preference pairs, PYR-PYR pre 20074, 16750 post 41548, 38056, PYR-PV pre 2132, 1513, post 4856, 4300. Data distribution shown in **Supplementary Fig. 11d** (**k**) Schematic depicting how PYR to PV interaction weights (arrows of different thickness) rearrange to provide selective inputs to PV cells after learning.

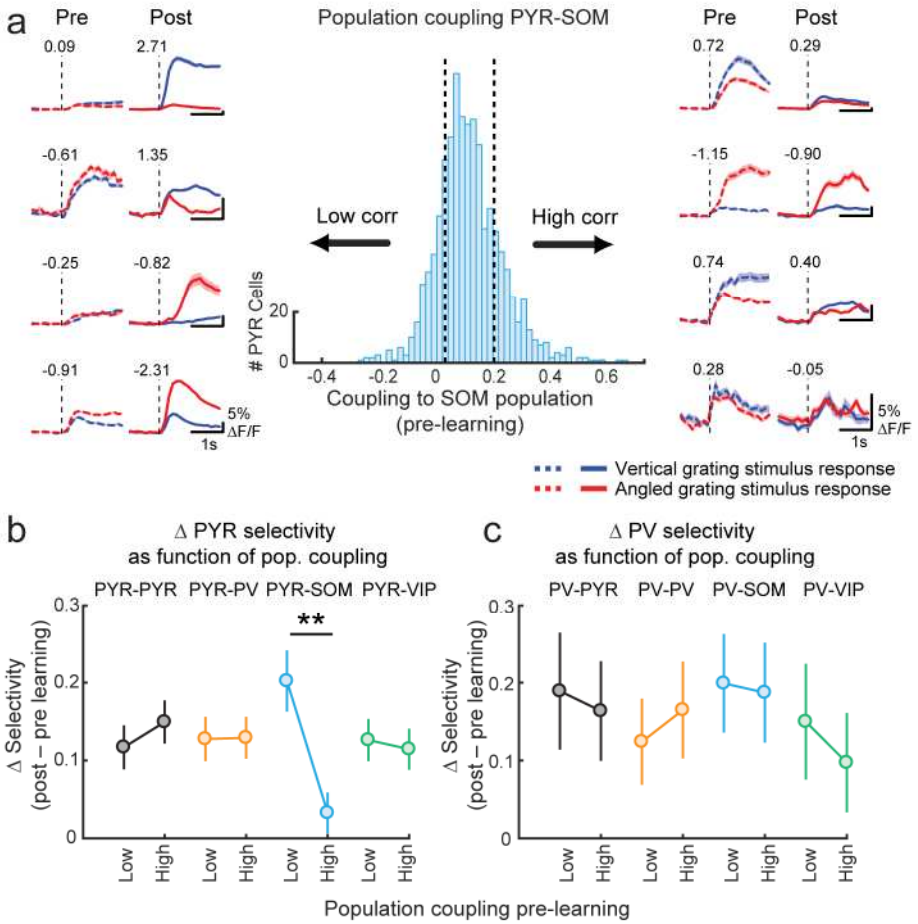

Figure 5. Degree of coupling with the SOM cell population before learning is related to PYR cell selectivity increase. (**a**) Centre: distribution of pre-learning noise correlations between individual PYR cells and the average activity of the SOM cell population, N = 1249 PYR cells. Vertical dashed lines denote top and bottom 20th percentiles. Left and right: 4 example cells each showing average grating responses pre- and post-learning of representative PYR cells with low (left) and high (right) pre-learning SOM cell population coupling. Numbers above traces indicate selectivity. (**b, c**) Difference in the absolute selectivity pre- and post-learning (Δselectivity) of PYR cells (**b**) and PV cells (**c**) with low and high (bottom and top 20th percentiles) coupling to the four cell populations. Wilcoxon rank-sum test, **, P = 0.001, N = 250 PYR cells (**b**) and 26 PV cells (**c**) in each group. Error bars represent SEM.

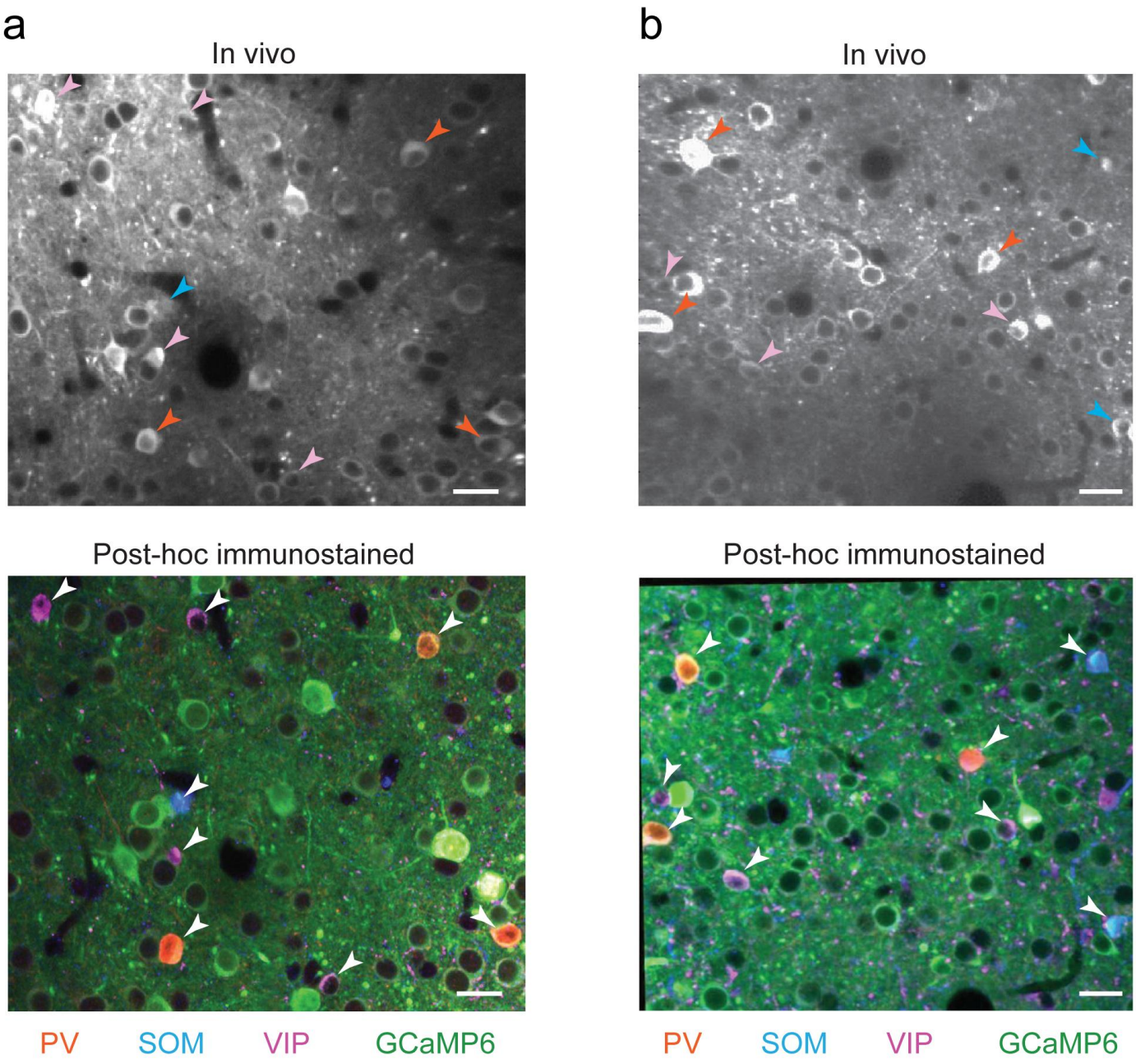

Supplementary Figure 1

Co-registration of in vivo two-photon images and immunohistochemically stained brain sections

(**a, b**) Top, example regions of in vivo images of GCaMP6f-labelled neurons. Bottom, same regions after post-hoc immunostaining for PV, SOM and VIP (red, blue and magenta respectively) and image registration to match the in vivo image. GCaMP6f label is shown in green. Corresponding interneurons are indicated by arrowheads. Scale bars, 20 μm. Image registration and cell matching was performed for each mouse (N=8).

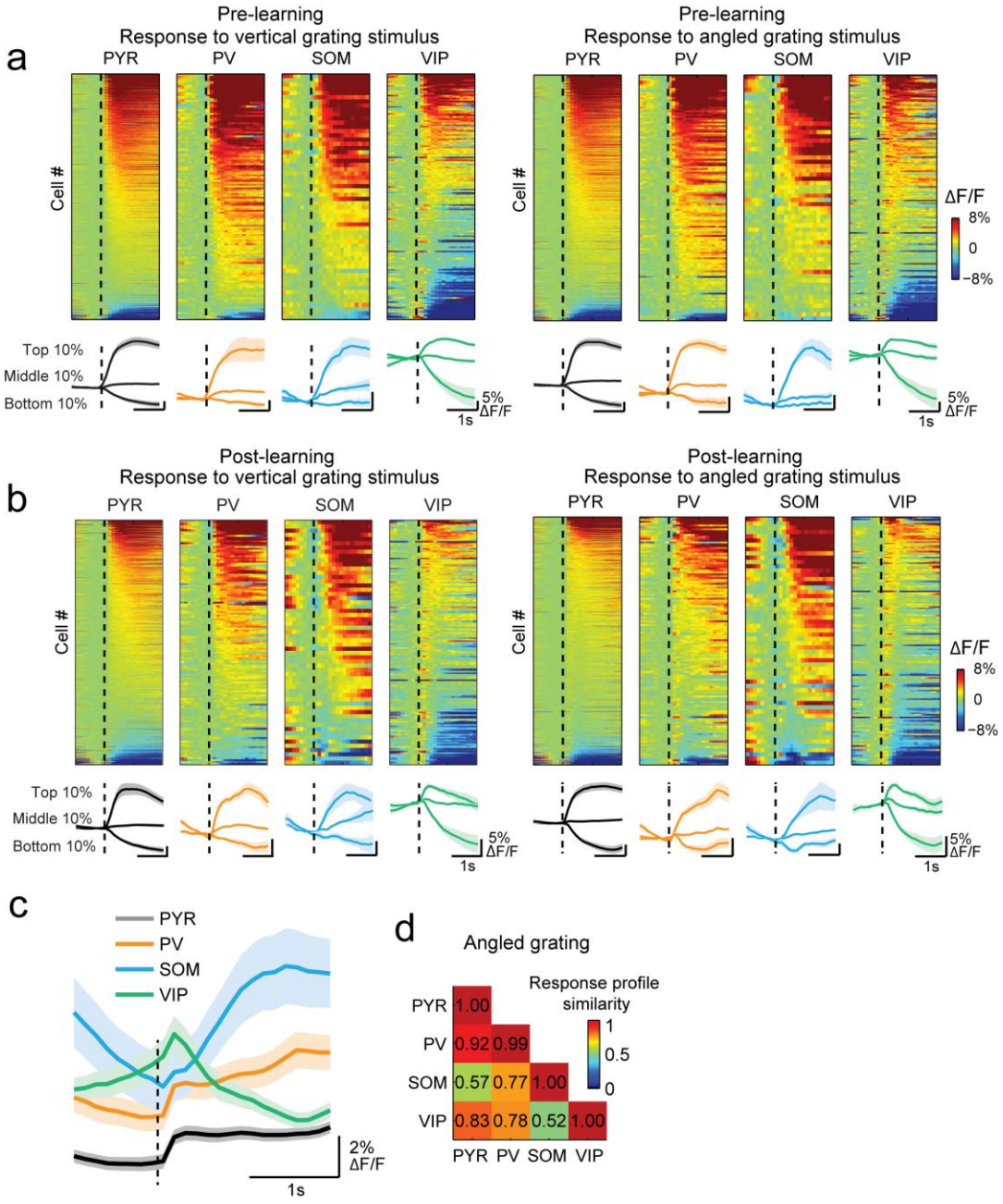

Supplementary Figure 2

Responses to the grating stimuli before and after learning

(**a, b**) Average responses of all recorded neurons of each cell type before (**a**) and after learning (**b**) to the vertical (left) and angled grating (right). Calcium responses are baseline corrected (subtraction of baseline ΔF/F -0.5 to 0 s before stimulus onset), and aligned to grating onset (dashed line). Cells are sorted by their average response amplitude 0-1 s from stimulus onset. Number of cells included in each plot: 1249, 132, 58 and 175 for PYR, PV, SOM and VIP, respectively. Bottom, average responses of cells from the top, middle and bottom 10th percentiles of grating-evoked response amplitudes of each cell class. (125, 13, 6 and 18 cells in each 10th percentile, respectively) Shaded area represents SEM here and elsewhere. (**c**) Average response to the angled grating of all cells from each cell class after learning. (**d**) Similarity of response profiles to the angled grating of all pairs of cell classes attained with a random forest decoder to classify single cells to one of two classes based on the shape of their average baseline-subtracted response profiles (see Online Methods). Response profile similarity score = 2 × (1- classification accuracy). Scores near 0 and 1 indicate low and high response profile similarity between two cell classes respectively.

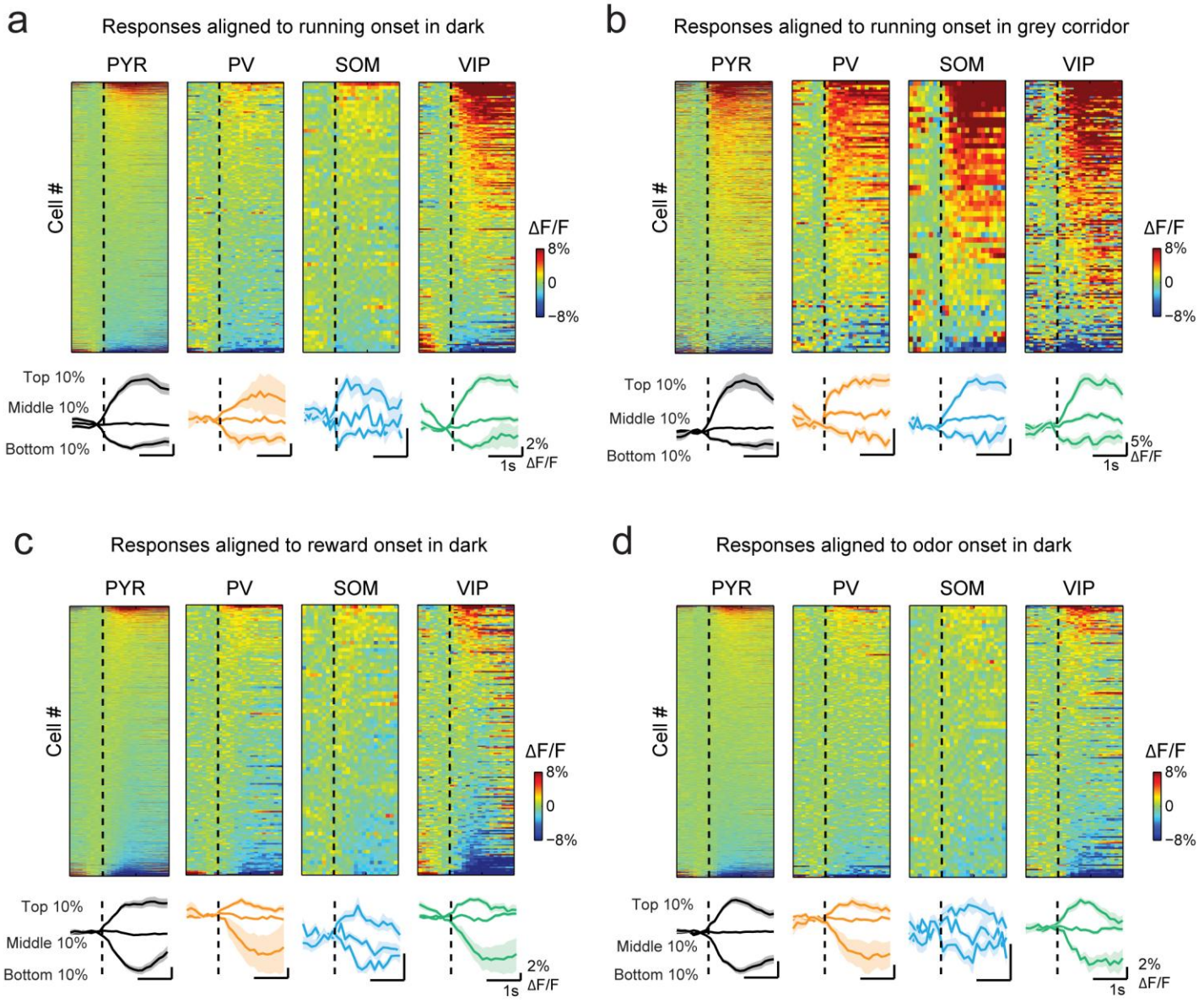

Supplementary Figure 3

Responses triggered by the onset of running, reward and odor

(**a**) Top, average responses to the onset of running in the dark of all recorded neurons of each cell type as the mouse performed an odor discrimination task in the dark (see Online Methods). Calcium responses are baseline corrected (subtraction of baseline ΔF/F -0.5 to 0 s before running onset), and aligned to running onset (dashed line). Cells are sorted by their average response amplitude 0-1 sec from onset. Number of cells included in a,c,d: 2795, 185, 75 and 192 and in b 1064, 121, 52, 156 for PYR, PV, SOM and VIP, respectively. Bottom, average responses of cells from the top, middle and bottom 10th percentiles of running onset-aligned response amplitudes of each cell class (in a,c,d: 208, 19, 8 and 19 cells and in b: 106, 12, 5 and 16 cells in each 10th percentile, respectively). Shaded area represents SEM here and elsewhere. Running onsets were defined as times where running speed of the mouse crossed 6 cm/s after being stationary for at least 0.5 s. (**b**) Responses aligned to onset of running in the grey corridor during the visual discrimination task, similar to (**a**). Only periods when mice were in the grey corridor for at least 0.5 s before and 1 s after running onset were selected, to minimize optic-flow related responses. (**c**) Responses aligned to reward onset during the odor discrimination task (see Online Methods), similar to (**a**). (**d**) Responses aligned to the non-rewarded odor onset during the odor discrimination task (see Online Methods), similar to (**a**).

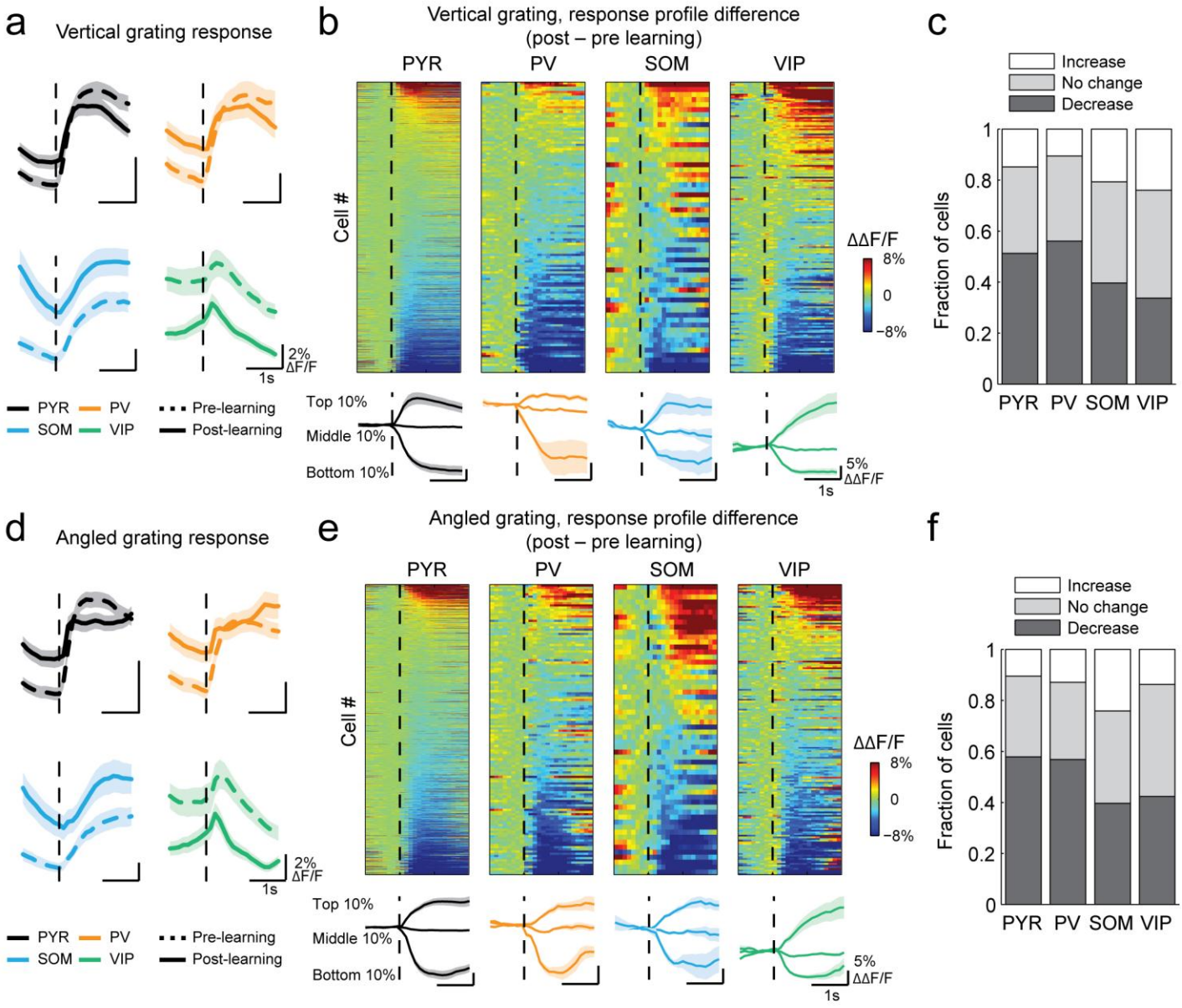

Supplementary Figure 4

Response changes during learning

(**a**, **d**) Average response profiles in response to vertical (**a**) and angled grating stimulus (**d**) of all cells from each cell class before (dashed line) and after (solid line) learning. Vertical dashed line indicates grating onset. Shaded area represents SEM, here and elsewhere. N = 1249, 132 PV, 58 SOM and 175 VIP cells here and below. (**b**, **e**) Top: Difference between post-learning and pre-learning response profiles in response to the vertical (**b**) and angled (**e**) grating stimuli for all cells of different cell classes. Responses were baseline corrected before subtracting (baseline -.5 to 0 sec before stimulus onset), are shown aligned to grating onset (dashed line), and color coded for Δ(ΔF/F). Bottom: average responses of cells from the top, middle and bottom 10th percentiles of the response differences shown on top. (**c**, **f**) Fractions of cells in which the response amplitude to the vertical (**c**) and angled (**f**) grating stimuli increased, decreased, or showed no difference from pre-to post-learning in the period 0-1 s from stimulus onset.

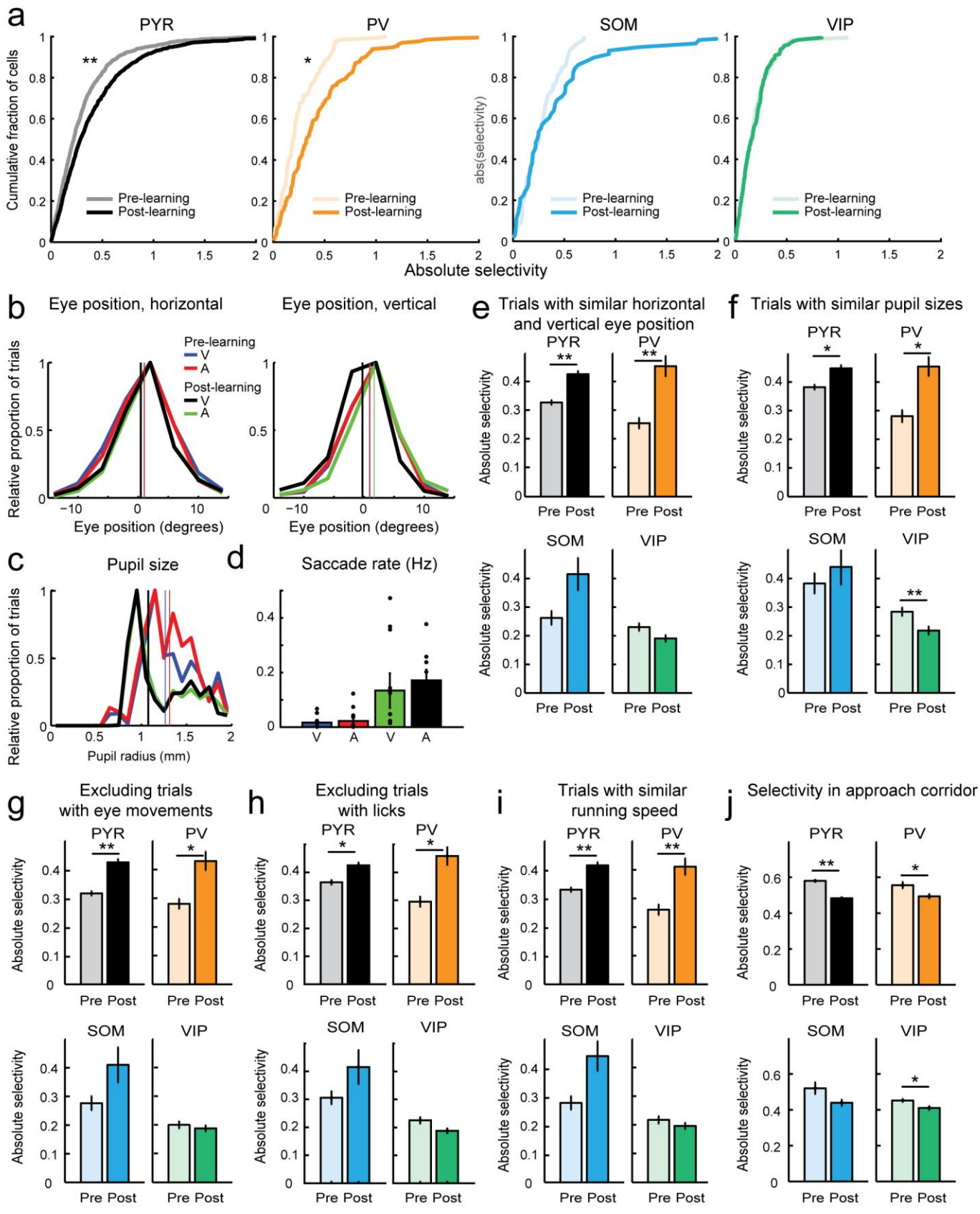
a
PYR
PV
SOM
VIP
Cumulative fraction of cells
abs(selectivity)
Pre-learning
Post-learning
Absolute selectivity
b
Eye position, horizontal
Eye position, vertical
Relative proportion of trials
Eye position (degrees)
c
Pupil size
Pupil radius (mm)
d
Saccade rate (Hz)
e
Trials with similar horizontal and vertical eye position
f
Trials with similar pupil sizes
Absolute selectivity
Pre Post
g
Excluding trials with eye movements
h
Excluding trials with licks
i
Trials with similar running speed
j
Selectivity in approach corridor

Supplementary Figure 5

Effect of eye position, pupil size, eye movements, running and licking on selectivity of responses

(**a**) Cumulative distribution of absolute selectivity of each cell class before and after learning. Sign test, **, $P < 0.001$; *, $P < 0.05$ here and below. (**b**) Distributions of average horizontal (nasal-temporal axis) and vertical (ventral-dorsal axis) eye positions and (**c**) pupil sizes of the contralateral eye in individual trials 0-1 s after onset of the vertical (V) and angled (A) grating, before and after learning. (**d**) Saccade rate 0-1 s after grating onset before and after learning. (**e-i**) Mean absolute selectivity of each cell class before and after learning (computed in the period of 0-1s after grating onset) after equalizing the distributions of horizontal and vertical eye positions in all conditions (**e**), after equalizing the distributions of pupil sizes (**f**), when excluding all trials with eye movements (**g**), when excluding all trials with licks (**h**), and after equalizing the distributions of running speed (**i**). Error bars are SEM. Numbers of cells recorded both pre- and post-learning: 1249 PYR, 132 PV, 58 SOM and 175 VIP cells, N = 8 mice. (**j**) Response selectivity in the approach corridor before and after learning.

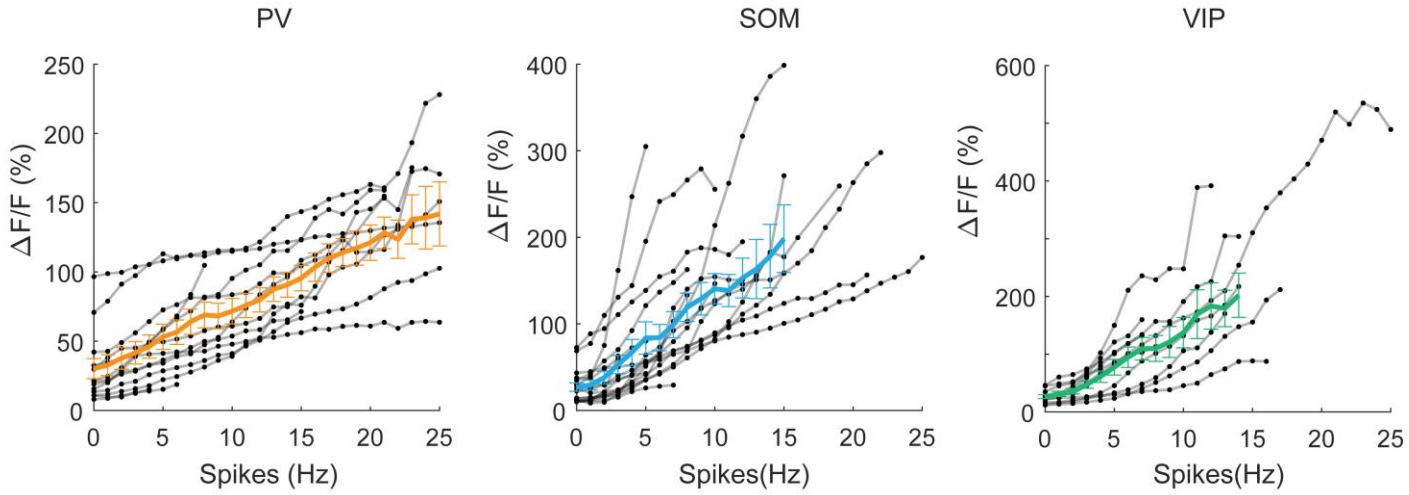

Supplementary Figure 6

Relationship between action potential firing rate and calcium transient size in simultaneous loose patch and GCaMP6f recordings from the three interneuron classes in visual cortex slices

Black lines are individual cells, colored lines are averages across cells, plotted for firing rate bins including at least five cells. Error bars represent SEM, PV = 13, SOM = 17 and VIP = 11 cells.

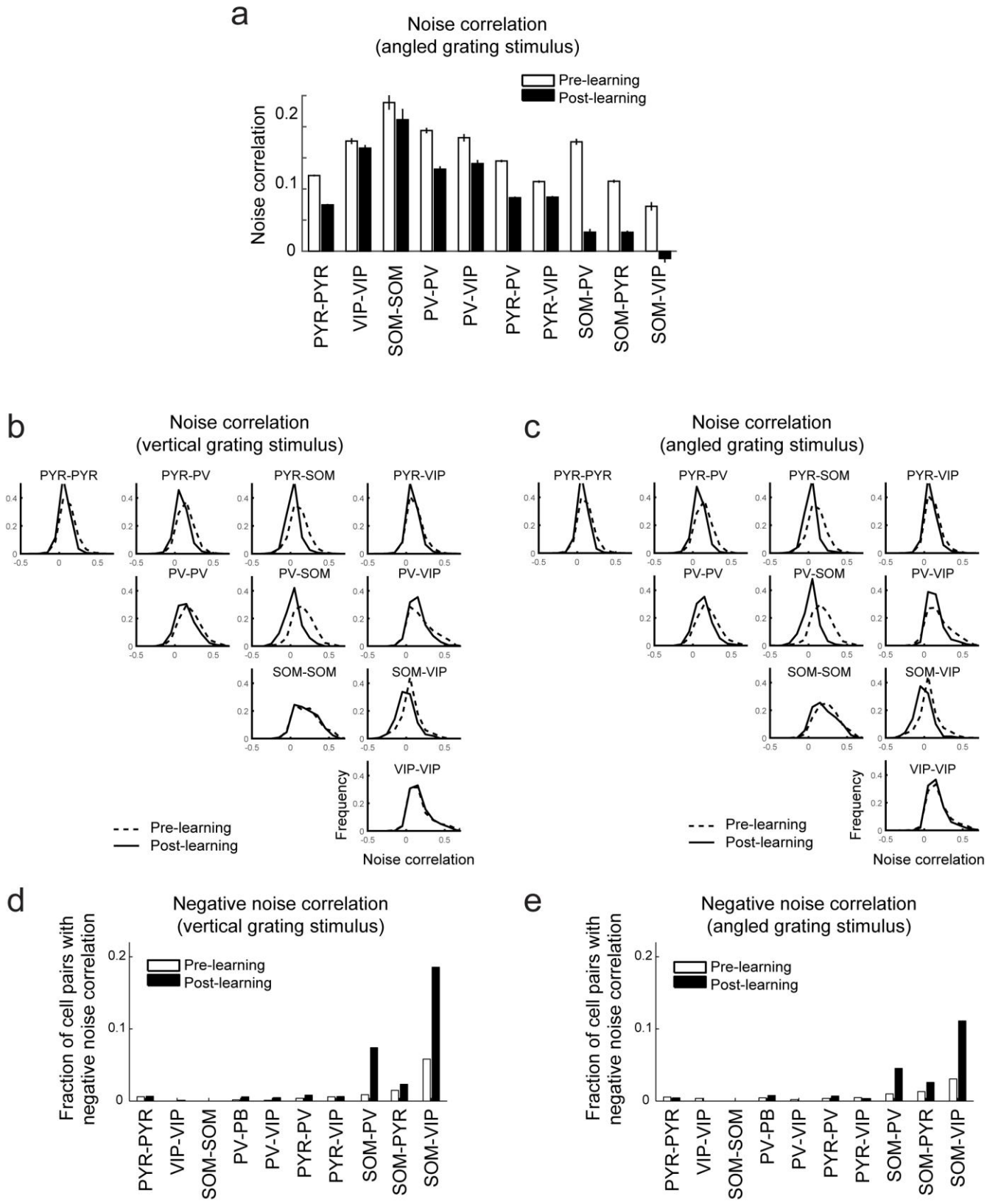
a
Noise correlation
(angled grating stimulus)
Pre-learning
Post-learning
Noise correlation
0.2
0.1
0
PYR-PYR
VIP-VIP
SOM-SOM
PV-PV
PV-VIP
PYR-PV
PYR-VIP
SOM-PV
SOM-PYR
SOM-VIP
b
Noise correlation
(vertical grating stimulus)
PYR-PYR
PYR-PV
PYR-SOM
PYR-VIP
PV-PV
PV-SOM
PV-VIP
SOM-SOM
SOM-VIP
VIP-VIP
Pre-learning
Post-learning
Frequency
Noise correlation
c
Noise correlation
(angled grating stimulus)
PYR-PYR
PYR-PV
PYR-SOM
PYR-VIP
PV-PV
PV-SOM
PV-VIP
SOM-SOM
SOM-VIP
VIP-VIP
Pre-learning
Post-learning
Frequency
Noise correlation
d
Negative noise correlation
(vertical grating stimulus)
Fraction of cell pairs with
negative noise correlation
Pre-learning
Post-learning
0.2
0.1
0
PYR-PYR
VIP-VIP
SOM-SOM
PV-PB
PV-VIP
PYR-PV
PYR-VIP
SOM-PV
SOM-PYR
SOM-VIP
e
Negative noise correlation
(angled grating stimulus)
Fraction of cell pairs with
negative noise correlation
Pre-learning
Post-learning
0.2
0.1
0
PYR-PYR
VIP-VIP
SOM-SOM
PV-PB
PV-VIP
PYR-PV
PYR-VIP
SOM-PV
SOM-PYR
SOM-VIP

Supplementary Figure 7

Changes in noise correlation during learning

(**a**) Top: Mean noise correlation measured during the angled grating response (0-1 s from stimulus onset) between cell pairs of each combination of cell classes, before and after learning. The number of cell pairs here and below in each cell class combination (pre, post-learning) was: PYR-PYR 77599, 66633, VIP-VIP 984, 776, SOM-SOM 201, 131, PV-PV 1646, 1316, PV-VIP 818, 702, PV-PYR 17496, 15029, PYR-VIP 14485, 11893, SOM-PV 1176, 828, SOM-PYR 7121, 5545, SOM-VIP 476, 364. Error bars represent SEM. (**b**, **c**) Distributions of noise correlation between cell pairs of each combination of cell classes during the vertical (**b**) or angled (**c**) grating response before and after learning. (**d**, **e**) Fraction of cell pairs with significantly negative noise correlation during the vertical (**d**) or angled (**e**) grating response before and after learning. Only neurons with significant responses to the grating were included in the analysis.

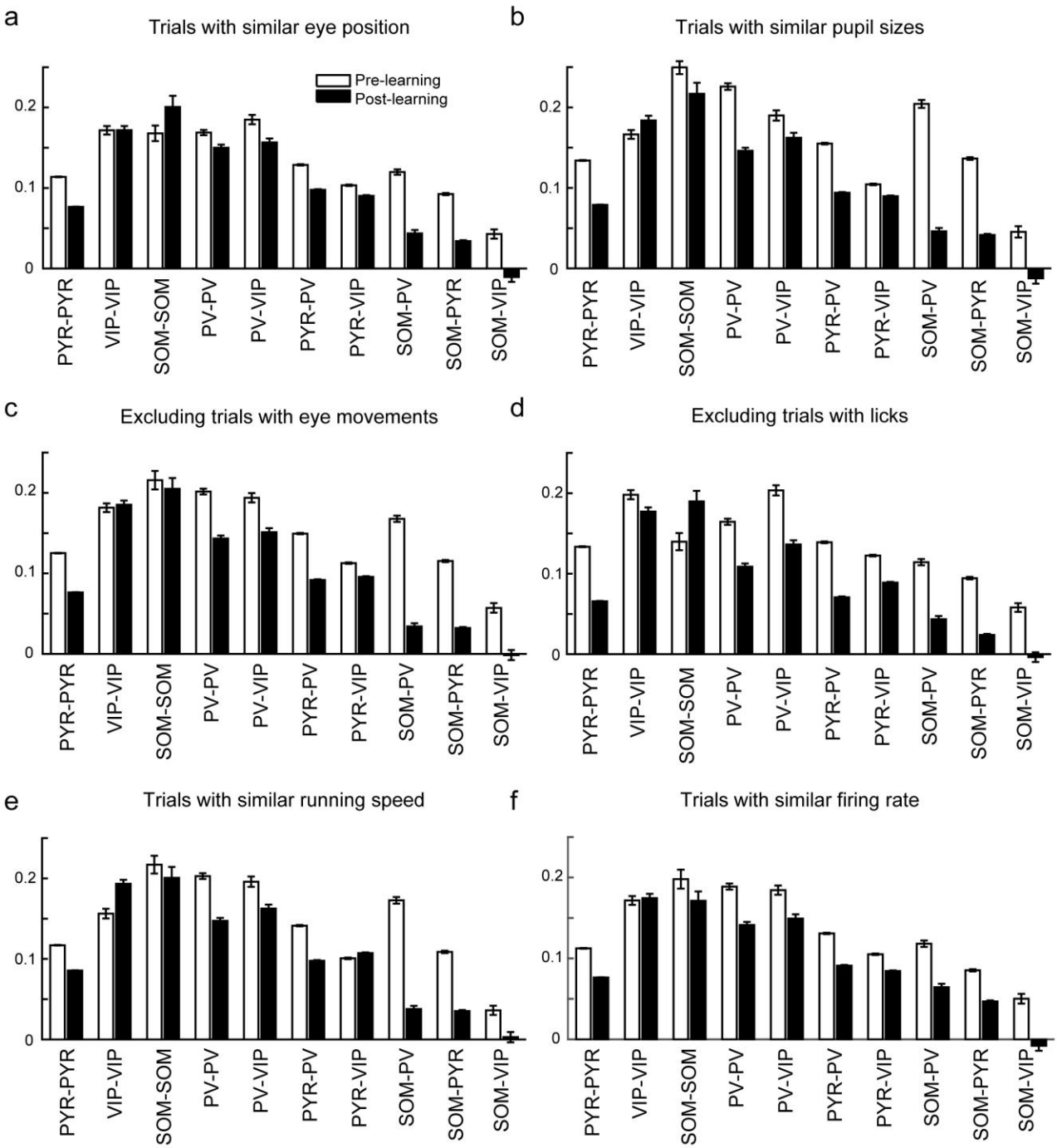

Supplementary Figure 8

Changes in eye position, pupil size, eye movements, running, licking and reductions in response strength cannot account for reduction in noise correlations with learning

Mean noise correlations measured during the vertical grating response (0-1 s from stimulus onset) after equalizing the distributions of eye position (**a**), pupil sizes (**b**), when excluding all trials with eye movements (**c**), when excluding all trials with licks (**d**), after equalizing the distributions of running speed (**e**), and after controlling for reductions in response strength (**f**). The number of cell pairs (pre, post-learning) was: PYR-PYR 77599, 66633, VIP-VIP 984, 776, SOM-SOM 201, 131, PV-PV 1646, 1316, PV-VIP 818, 702, PV-PYR 17496, 15029, PYR-VIP 14485, 11893, SOM-PV 1176, 828, SOM-PYR 7121, 5545, SOM-VIP 476, 364. Error bars represent SEM.

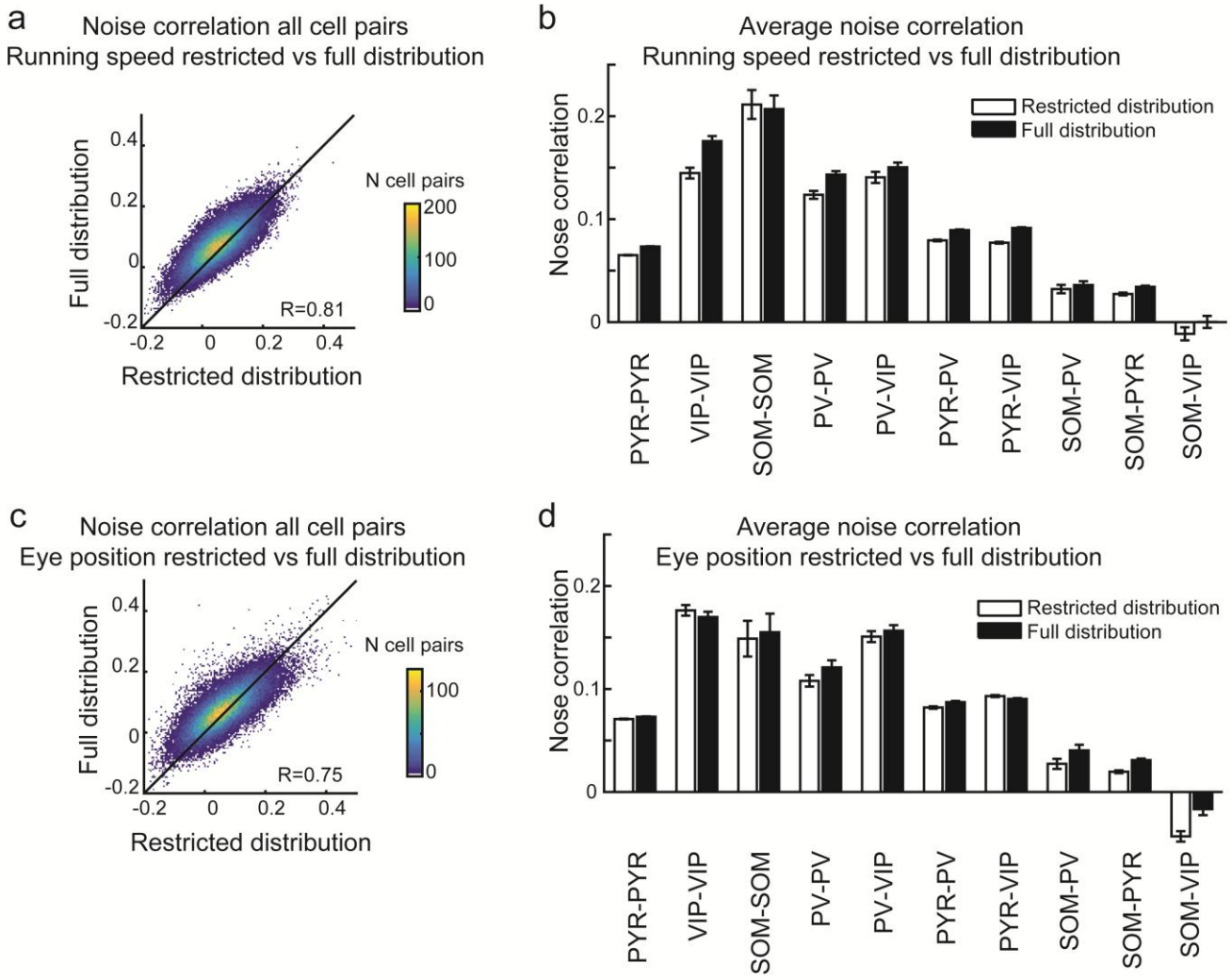

Supplementary Figure 9

Variability in running speed, visual flow and eye position did not make a large contribution to measured noise correlation

(**a, b**) Variability in running speed and coupled visual flow was reduced by sampling trials only from the middle 50% of running speed distribution (25th to 75th percentile), and compared to an equal number of trials sampled randomly from the full distributions. Noise correlations obtained in these two conditions were very similar, both for individual cell pairs (**a**), and for average noise correlations between specific cell classes (**b**). (**c, d**) Same analysis for eye position. R indicates Pearson correlation coefficient. The number of cell pairs (pre, post-learning) was: PYR-PYR 77599, 66633, VIP-VIP 984, 776, SOM-SOM 201, 131, PV-PV 1646, 1316, PV-VIP 818, 702, PV-PYR 17496, 15029, PYR-VIP 14485, 11893, SOM-PV 1176, 828, SOM-PYR 7121, 5545, SOM-VIP 476, 364. Error bars represent SEM.

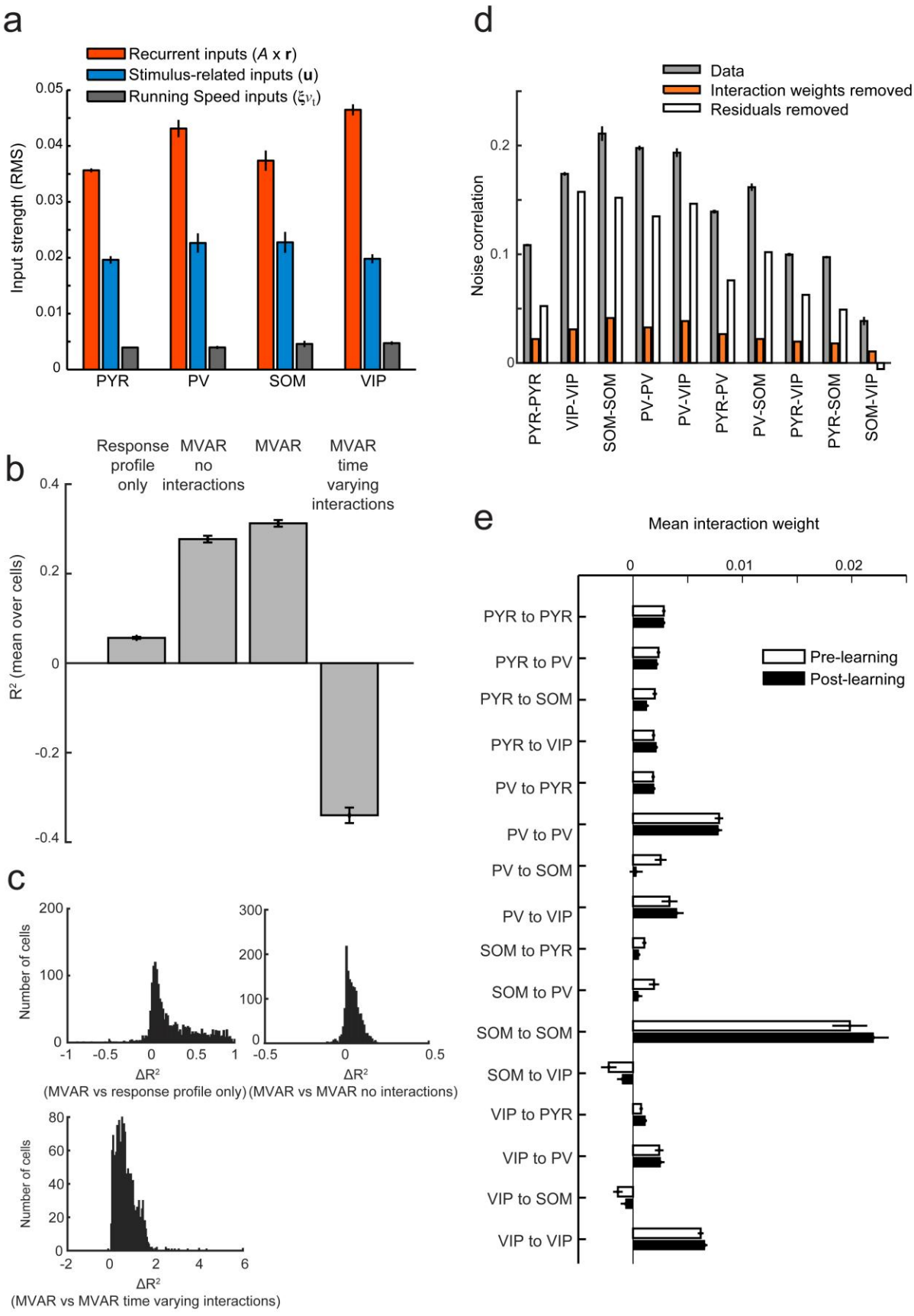
a
Recurrent inputs (A x r)
Stimulus-related inputs (u)
Running Speed inputs (ξν_t)
Input strength (RMS)
0.05
0.04
0.03
0.02
0.01
0
PYR
PV
SOM
VIP
b
Response profile only
MVAR no interactions
MVAR
MVAR time varying interactions
R² (mean over cells)
0.4
0.2
0
-0.2
-0.4
c
Number of cells
200
100
0
-1
-0.5
0
0.5
1
ΔR²
(MVAR vs response profile only)
300
200
100
0
-0.5
0
0.5
ΔR²
(MVAR vs MVAR no interactions)
Number of cells
80
60
40
20
0
-2
0
2
4
6
ΔR²
(MVAR vs MVAR time varying interactions)
d
Data
Interaction weights removed
Residuals removed
Noise correlation
0.2
0.1
0
PYR-PYR
VIP-VIP
SOM-SOM
PV-PV
PV-VIP
PYR-PV
PV-SOM
PYR-VIP
PYR-SOM
SOM-VIP
e
Mean interaction weight
0
0.01
0.02
PYR to PYR
PYR to PV
PYR to SOM
PYR to VIP
PV to PYR
PV to PV
PV to SOM
PV to VIP
SOM to PYR
SOM to PV
SOM to SOM
SOM to VIP
VIP to PYR
VIP to PV
VIP to SOM
VIP to VIP
Pre-learning
Post-learning

Supplementary Figure 10

Multivariate autoregressive (MVAR) linear dynamical system model

(**a**) Root mean square (RMS) of the strength of the three types of inputs in the MVAR model for all cells of each class (N = 1249 PYR, 132 PV, 58 SOM and 175 VIP cells). Running speed has relatively small contributions. (**b**) Cross-validated R^2 (mean over cells, N = 1614) for models of increasing complexity. The MVAR model performed better than the other models (all Ps < 10^{-150}, sign test). The small increase in R^2 when interactions were included indicates that the cross-validated prediction performance improved despite the considerable increase in model complexity (approximately 40,000 extra parameters per animal), which would be expected to lead to a large drop in performance due to overfitting if interactions were not informative. In contrast, the negative R^2 values for the model that included time-varying interactions indicate that the inclusion of time-varying interaction weights leads to overfitting on the training data. (**c**) Histograms of the difference in R^2 obtained from the MVAR model and each of the other models tested in (**b**) for each cell. In all comparisons the majority of cells performed better with the MVAR model (positive ΔR^2 in 93%, 83% and 99% of cells compared to models with average response profiles only, MVAR without interactions and MVAR with time varying interactions respectively). (**d**) Average pre-learning noise correlations observed (grey), after setting interaction weights to zero (orange), and after shuffling residuals (white), similar to **Fig. 4c**. The number of cell pairs was: PYR-PYR 77599, VIP-VIP 984 SOM-SOM 201, PV-PV 1646, PV-VIP 818, PV-PYR 17496, PYR-VIP 14485, SOM-PV 1176, SOM-PYR 7121, SOM-VIP 476. (**e**) Mean interaction weights obtained from the MVAR model fit pre-and post-learning. Error bars represent SEM.

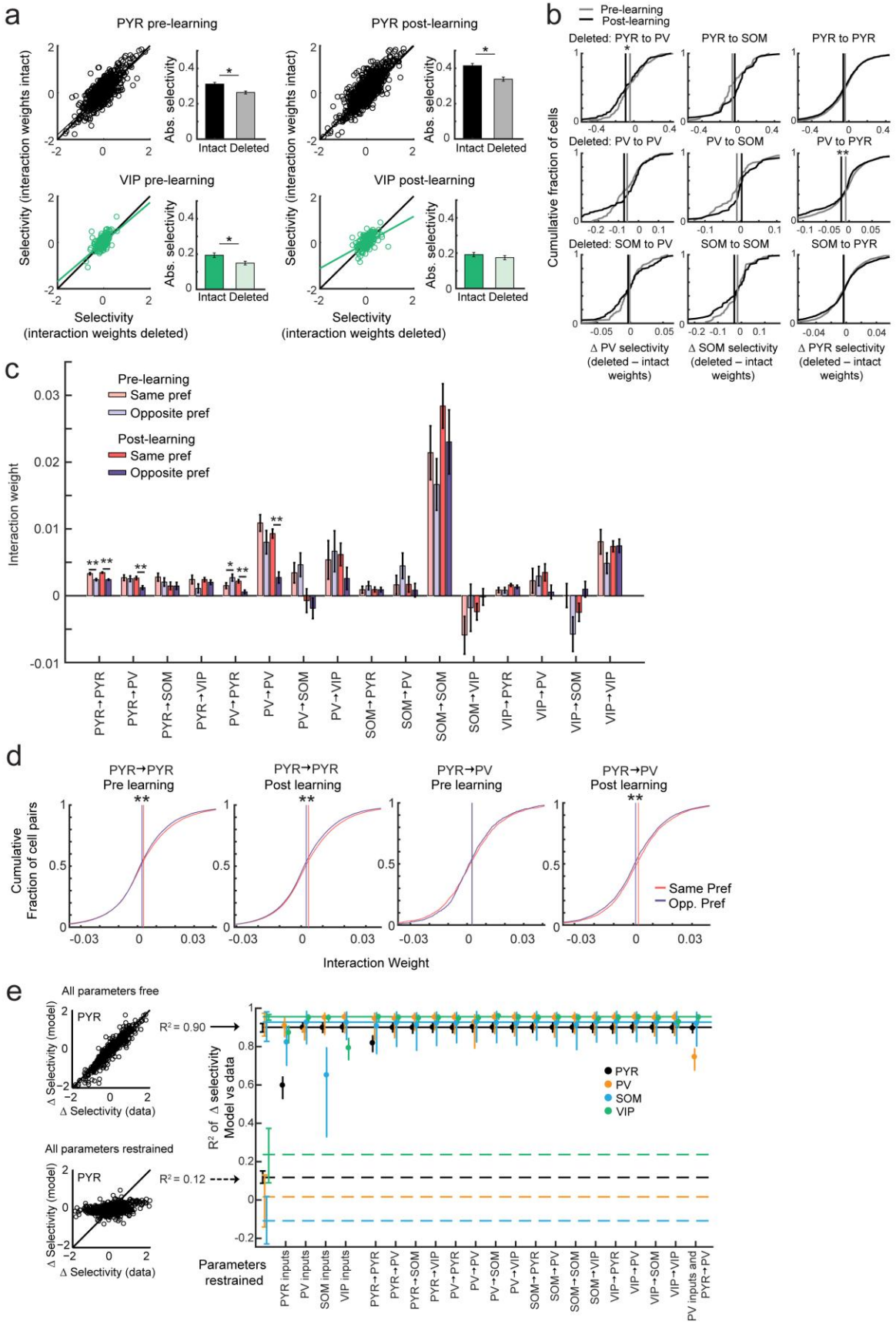
a
PYR pre-learning
PYR post-learning
VIP pre-learning
VIP post-learning
Selectivity (interaction weights intact)
Selectivity (interaction weights deleted)
Abs. selectivity
Intact Deleted
b
Pre-learning
Post-learning
Deleted: PYR to PV
PYR to SOM
PYR to PYR
Deleted: PV to PV
PV to SOM
PV to PYR
Deleted: SOM to PV
SOM to SOM
SOM to PYR
Cumullative fraction of cells
Δ PV selectivity (deleted – intact weights)
Δ SOM selectivity (deleted – intact weights)
Δ PYR selectivity (deleted – intact weights)
c
Pre-learning
Same pref
Opposite pref
Post-learning
Same pref
Opposite pref
Interaction weight
PYR→PYR
PYR→PV
PYR→SOM
PYR→VIP
PV→PYR
PV→PV
PV→SOM
PV→VIP
SOM→PYR
SOM→PV
SOM→SOM
SOM→VIP
VIP→PYR
VIP→PV
VIP→SOM
VIP→VIP
d
PYR→PYR Pre learning
PYR→PYR Post learning
PYR→PV Pre learning
PYR→PV Post learning
Cumulative Fraction of cell pairs
Same Pref
Opp. Pref
Interaction Weight
e
All parameters free
All parameters restrained
PYR
Δ Selectivity (model)
Δ Selectivity (data)
R² = 0.90
R² = 0.12
R² of Δ selectivity Model vs data
PYR
PV
SOM
VIP
Parameters restrained
PYR inputs
PV inputs
SOM inputs
VIP inputs
PYR→PYR
PYR→PV
PYR→SOM
PYR→VIP
PV→PYR
PV→PV
PV→SOM
PV→VIP
SOM→PYR
SOM→PV
SOM→SOM
SOM→VIP
VIP→PYR
VIP→PV
VIP→SOM
VIP→VIP
PV inputs and PYR→PV

Supplementary Figure 11

Effect of deleting and constraining parameters in the MVAR model

(**a**) Effect of deleting all interaction weights between cells in the MVAR model on selectivity in PYR (top) and VIP cells (bottom) before (left) and after (right) learning. N = 1249 PYR, 175 VIP, 132 PV and 58 SOM cells here and below. Bars indicate average absolute selectivity with weights intact and deleted. *, $P < 10^{-3}$. Sign test comparing intact and deleted conditions, PYR cells pre-learning $P < 10^{-11}$, post-learning $P < 10^{-17}$, VIP cells pre-learning $P < 10^{-3}$, post-learning $P > 0.05$. Error bars represent SEM. (**b**) Effect of deleting specific interaction weights onto PV, SOM and PYR cells on their selectivity pre- and post-learning (Δselectivity). Same data as in **Fig. 4g, h, i**, showing distributions. Vertical lines indicate mean. **, $P < 10^{-3}$, *, $P < 0.05$ here and below. (**c**) Interaction weights in MVAR model before and after learning for cell pairs with the same or opposite stimulus-input preference. Error bars represent SEM. Wilcoxon rank-sum test, N interaction weights range from 50 to 41548. (**d**) Distribution of interaction weights in MVAR model before and after learning for PYR-PYR and PYR-PV cell pairs with the same or opposite stimulus-input preference, similar to **Fig. 4j**. Vertical lines indicate mean. N interaction weights pre- and post-learning for same or opposite preference pairs, PYR-PYR pre 20074, 16750 post 41548, 38056, PYR-PV pre 2132, 1513, post 4856, 4300 (**e**) MVAR jointly fit to the pre- and post-learning data, while constraining specific parameters (stimulus inputs or interaction weights) to remain fixed across learning and allowing others to vary. Holding all or none of the parameters fixed gave poor or good fits of selectivity changes during learning respectively (left, example R^2 with all parameters free or restrained shown for PYR cells, values for all cell classes indicated by horizontal lines in right panel). When stimulus inputs to PYR or SOM cells were held fixed over learning, the model failed to fully capture their respective selectivity changes (right, inputs restrained, bootstrap test with resampling of residuals (see Online Methods) on the difference between model with all parameters free compared to model with parameters fixed, P-values < 0.002). In contrast, the relatively large changes in PV selectivity were not significantly disrupted when stimulus inputs to PV cells were held fixed ($P = 0.4$), indicating that changes in interaction weights and stimulus inputs to other cell types are sufficient to account for the selectivity changes observed in PV cells during learning. The model with VIP inputs fixed also fully captured VIP selectivity changes ($P = 0.71$), likely due to the selectivity changes in these cells being very small. Furthermore, simultaneously fixing both PV inputs and PYR to PV weights significantly impaired the model to fully capture PV selectivity changes (both relative to the full model ($P = 0.03$) and relative to the model with fixed PV inputs alone ($P < 0.002$). Error bars represent 90% confidence intervals from bootstrapping with resampling of cells.

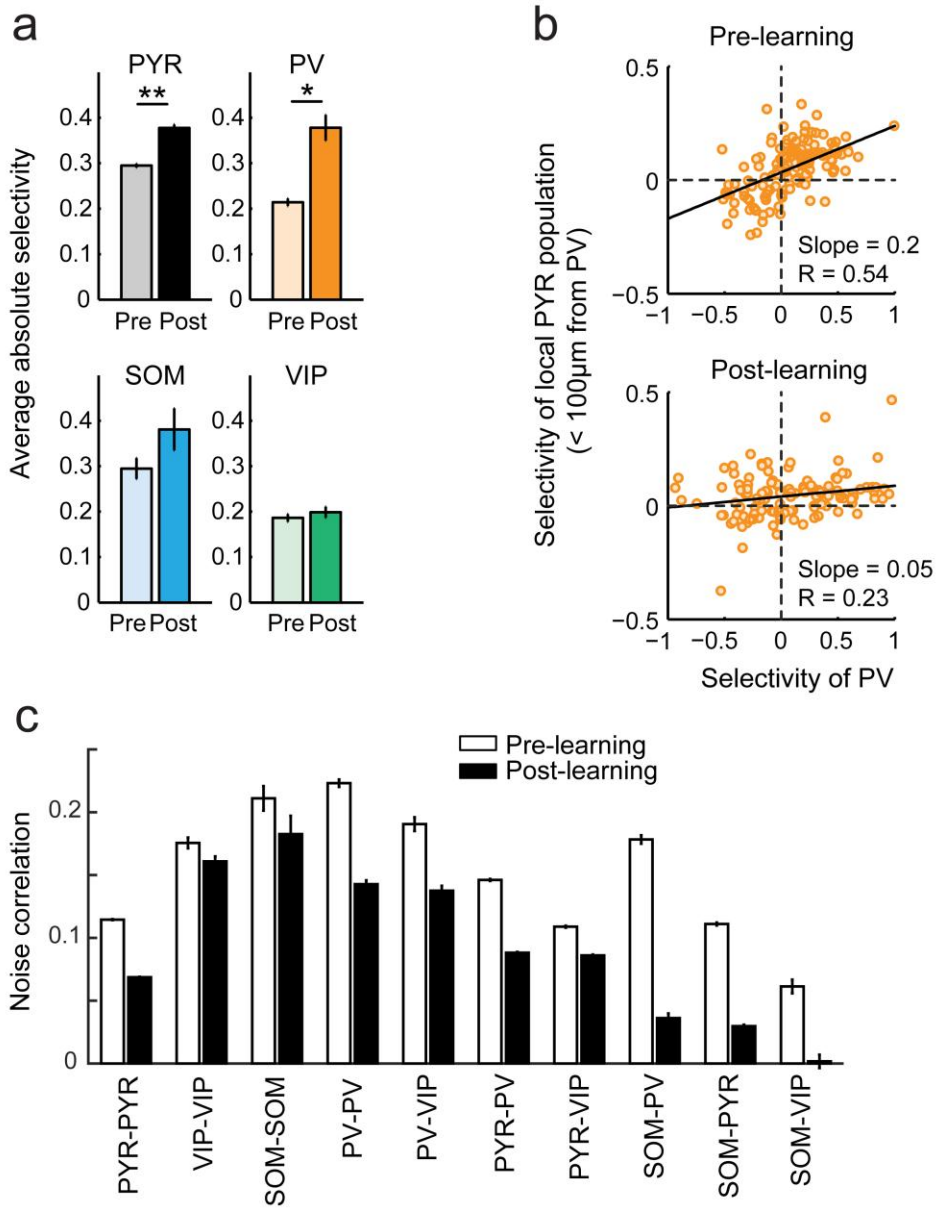

Supplementary Figure 12

After correcting for neuropil contamination, learning-related changes in selectivity as well as changes in interactions remain largely unchanged

We subtracted from each ROI the average fluorescence of all pixels within a neuropil mask surrounding the cell (see Online Methods) and repeated key analyses. Panels **a** and **b** reproduce Figure 2d and g. 1249 PYR, 132 PV, 58 SOM and 175 VIP cells in a and b. R is Pearson correlation coefficient. Panel **c** reproduces Figure 3c. *, $P < 10^{-2}$, **, $P < 10^{-9}$, sign test, error bars represent SEM. The number of cell pairs in each cell class combination (pre, post-learning) was: PYR-PYR 74581, 64921, VIP-VIP 1166, 907, SOM-SOM 215, 99, PV-PV 1731, 1369, PV-VIP 790, 718, PV-PYR 17792, 15238, PYR-VIP 14681, 12009, SOM-PV 1250, 690, SOM-PYR 7112, 4952, SOM-VIP 455, 377.

a) Primary antibodies

Target	Host	Dilution	Supplier
Parvalbumin	Goat	1/500	Swant (PVG-213)
Parvalbumin	Mouse	1/1000	Swant (PV 235)
Vasoactive intestinal peptide	Rabbit	1/500	ImmunoStar anti-VIP (#20077)
Somatostatin	Rat	1/200	Millipore (MAB354)

b) Secondary antibodies

Genotype	Primary	Secondary	Code number
WT	Mouse-anti PV	DyLight 405	715-475-150
	Rabbit-anti VIP	Rhodamine Red X	711-295-152
	Rat-anti SOM	Alexa 647	712-605-153
PV-tdTomato	Mouse-anti PV	Alexa 594	715-585-151
	Rabbit-anti VIP	Alexa 647	711-605-152
	Rat-anti SOM	DyLight 405	712-475-153
VIP-tdTomato	Goat-anti PV	DyLight 405	705-475-147
	Rabbit-anti VIP	Rhodamine Red X	711-295-152
	Rat-anti SOM	Alexa 647	712-605-153

Supplementary Table 1. **a, b**) Primary and secondary antibodies used in this study. All antibodies were applied in blocking buffer. All secondary antibodies were from Jackson ImmunoResearch and were used at 1/200 dilution.

a) Numbers and percentages of immuno-labelled cells that were also identified as belonging to the same interneuron class by transgenic labelling:

Genotype	**Immuno +**	**Also tdTomato +**	**Percent**
PV	250	236	94.4%
SOM	167	164	98.2%
VIP	152	139	91.4%

b) Numbers and percentages of transgenically labelled cells that were also identified as belonging to the same interneuron class by immunostaining:

Genotype	**tdTomato +**	**Also Immuno +**	**Percent**
PV	312	289	92.6%
SOM	278	195	70.1%
VIP	233	188	85.4%

Supplementary Table 2. **a, b**) Measure of overlap of labelling by immunostaining and transgenic mouse lines.